

Article

Influence of Fluvial Discharges and Tides on the Salt Wedge Position of a Microtidal Estuary: Magdalena River

Jhonathan R. Cordero-Acosta ^{*}, Luis J. Otero Díaz  and Aldemar E. Higgins Álvarez

Research Group in Geosciences—GEO4, Department of Physics and Geosciences, Universidad del Norte, Km. 5 Vía Puerto Colombia, Barranquilla 080001, Colombia; ljotero@uninorte.edu.co (L.J.O.D.)

* Correspondence: ajhonathan@uninorte.edu.co

Abstract: The linkage between the salt wedge, tidal patterns, and the Magdalena River discharge is established by assessing the ensuing parameters: stratification (ϵ), buoyancy frequency (β), potential energy anomaly (φ), Richardson number by layers (RL), and bottom turbulent energy production (P). The salinity, temperature, density, and water velocity data utilized were derived from MOHID 3D, a previously tailored and validated model for the Magdalena River estuary. To grasp the dynamics of the river, a flow regime analysis was conducted during both the wet and dry climatic seasons of the Colombian Caribbean. The utilization of this model aimed to delineate the estuary's spatial reach, considering flow rates spanning from 2000 to 6500 m³/s across two tidal cycles. This approach facilitates the prediction of the position, stability, and stratification degree of the salt front. Among the conclusions drawn, it is highlighted that: 1. The river flow serves as the principal conditioning agent for the system, inducing a strong estuary response to weather stations; 2. The extent of wedge intrusion and the river discharge exhibit a non-linear, inversely correlation; 3. Tidal waves cause differences of up to 1000 m in the horizontal extent of the wedge; 4. Widespread channel erosion occurs during the rainy season when the salt intrusion does not exceed 2 km; 5. Flocculation processes intensify during the transition between the dry and wet seasons; 6. The stability of the salt layering and the consolidation of the FSI-TMZ are contingent upon the geometric attributes of the channel.

Keywords: Magdalena River estuary; saline wedge estuary; saline wedge interannual variability; discharge–salinity relationship; Magdalena River mouth siltation



Citation: Cordero-Acosta, J.R.; Otero Díaz, L.J.; Higgins Álvarez, A.E. Influence of Fluvial Discharges and Tides on the Salt Wedge Position of a Microtidal Estuary: Magdalena River. *Water* **2024**, *16*, 1139. <https://doi.org/10.3390/w16081139>

Academic Editor: Bommanna Krishnappan

Received: 11 November 2023

Revised: 15 December 2023

Accepted: 19 December 2023

Published: 17 April 2024



Copyright: © 2024 by the authors. Licensee MDPI, Basel, Switzerland. This article is an open access article distributed under the terms and conditions of the Creative Commons Attribution (CC BY) license (<https://creativecommons.org/licenses/by/4.0/>).

1. Introduction

The circulation of water and sediment within estuaries is regulated by the density gradient between fresh and saltwater [1]. These density variations give rise to a horizontal baroclinic gradient that strives to equalize the free surface level and the isopycnals [2]. As a result, a bidirectional water flow is initiated, commonly referred to as estuarine circulation. This process can be categorized based on whether the net volume outflow, which is associated with gravitational circulation, exceeds or falls below the net volume inflow [3].

The interaction of river discharge, waves, currents, tidal patterns, and geomorphological factors collectively shapes the stratification and mixing dynamics of estuaries. In regions characterized by weak vertical stratification, such as tidal estuaries, the mixture of brackish water is uniform [4,5]. On the contrary, estuaries that are highly stratified encounter a constrained vertical mixing, resulting in the formation of a salt wedge [6,7]. Salt wedge estuaries are frequently present at the mouths of microtidal coastal rivers, where the river outflow suppresses the effects of tidal mixing [8]. In this scenario, with an increasing river flow, the freshwater outflow prevails, forcing the denser saltwater downstream. In low-discharge seasons, the tidal influx is amplified compared to the outflow, leading in a greater depth of salt wedge penetration upstream. This behavior highlights the river-controlled nature of most salt wedge estuaries, which can either facilitate or impede the input of

seawater [9–12]. It is important to emphasize the existence of tide-controlled estuaries that exhibit a time-dependent salt wedge development. The estuary of the São Francisco River in Northeast Brazil provides a suitable illustration [13].

Estuarine stratification is associated with the disruption of vertical transport mechanisms pertaining to nutrients and sediments, and it carries meaningful consequences for the productivity and functioning of these ecosystems [14,15]. Indeed, the salt wedge can lead to the occurrence of bottom hypoxia (low oxygen levels) or anoxia (complete lack of oxygen), negatively impacting benthic organisms [16]. The turbidity maximum zone (TMZ) is another essential factor in estuarine circulation. Positioned proximal to the upper boundary of the salt intrusion, this zone exhibits higher concentrations of finely suspended sediment when compared to those present in either the river or downstream areas of the estuary [17]. Intense flocculation processes occur in the TMZ, establishing a strong connection between the TMZ and estuarine siltation [18–21].

Fluvial estuaries, due to their location, have historically functioned as seaports and hubs for international trade. However, certain estuaries experience an increase in siltation rate that necessitates dredging channels to ensure and maintain ship navigability [22–24]. The Barranquilla seaport, located within the estuary of the Magdalena River (MRE), holds a vital role in the economic development of the city and its neighboring regions. This is mainly due to its distinction of having the largest number of terminals for international trade in Colombia [25,26]. Nonetheless, the seaport's operability encounters challenge due to the difference between the maximum bed sedimentation rates (2625 mm/year) and the maximum erosion rates (1450 mm/year), which is almost a twofold magnitude difference [20]. Hence, in order to maintain a minimum draught of 10 m, dredging operations are required [27]. The dredging procedure incurs high operational and logistical costs and does not offer a long-term solution. Moreover, it is conducted in disagreement with natural sedimentation patterns, rendering it an unsustainable approach [23,28].

The MRE is a microtidal saline wedge conditioned by the river discharge [29,30]. The sedimentation mechanisms are driven by the flocculation of suspended particles in the TMZ. The growth of the TMZ is correlated with a decrease in the bottom frictional energy of the water column during saline stratification, coupled with an increase in sediment availability. The decrease in bottom friction corresponds to the loss of the river's capacity for sediment resuspension, leading to the settling of flocs [31–33]. As previously noted, the displacement of the saline wedge is controlled by the energy of the Magdalena River. This results in heightened stratification during low-discharge periods, when tidal and wave energy have a greater impact. Between 1997 and 1998, during the dry season of the warm phase of the El Niño Southern Oscillation (ENSO), it was estimated to have a maximum saltwater penetration of 20 km upstream. Historical minimum flows, measuring around $\sim 2000 \text{ m}^3/\text{s}$, were recorded during this period. Conversely, during the wet season of the cold phase of the ENSO (between 1999 and 2000), the river outflow ranged from $10,000 \text{ m}^3/\text{s}$ to $14,000 \text{ m}^3/\text{s}$, enclosing the salt wedge extension within the first kilometer of the mouth [34].

A robust statistical correlation exists between the freshwater–saltwater interface (FSI) and the turbidity maximum zone (TMZ) location [31]. Consequently, comprehending the dynamics of stratification not only provides valuable insights into the position of the FSI, but also facilitates inferences concerning the spatial localization of the TMZ [34]. Furthermore, studying the behavior of the saline wedge can uncover opportunities to take advantage of the salinity gradient as a local energy source through the method of Reverse Electrodialysis (RED) [35,36], all of this while not overlooking the ecological significance of estuaries as an ecosystem rich in essential nutrients for vegetation and fauna [37–39]. This research aims to explore the effects of tidal patterns and seasonal fluctuations in river discharge on mixing dynamics, stratification, and the FSI's spatial distribution as a predictive indicator of the TMZ's formation. In this sense, our primary objective is to evaluate and delineate the specific regions where flocculation processes are expected to be intensified.

2. Study Area

The MRE is located on the Caribbean coast of Colombia. It is formed by the confluence of the Magdalena River (MR) and the Caribbean Sea. Due to its concentration of suspended sediment (CSS), it is classified as turbid and extremely turbid during high-flow seasons ($CSS \leq 11.450$ mg/L) [31,39]. This phenomenon is primarily attributed to human intervention, the steep topographical features, and the substantial precipitation in the upper reaches of the basin, resulting in high erosion and sedimentation rates. In comparison to other tributaries in the Caribbean Sea, the MR contributes the highest volume of suspended sediment (142.6×10^6 tons/year) [40,41]. Globally, the MR is ranked as the seventh highest in sediment yield, surpassing well-known rivers such as the Amazon (190 ton/ Km^2 year) or the Orinoco (140 ton/ Km^2 year) [42]. Since the construction of jetties in 1936 and subsequent modifications made until 2009, the water flow velocity and sediment transport capability of the river have increased [29,43]. This has led to a gradual deepening of the bed and cyclical changes between the erosive (310 mm/year) and sedimentation (293 mm/year) states on the inter-annual and intra-annual scales [20]. The climate exhibits two prevailing seasons: a wet season that lasts from May to December and a dry season that spans from January to April. These seasons are defined by the east trade winds and the oscillation of the Intertropical Convergence Zone (ITCZ) [44,45]. The winds have an average speed of 3.9 m/s, primarily blowing from the northeast for 42.7% of the year and from the north for 25% of the year [29]. The significant wave height, also originating from the northeast, is 2.2 ± 1.1 m, with a mean period (T) of 6.7 ± 2.3 s. The maximum wave heights can reach up to 4.5 m during extreme weather events, such as the one that occurred in 2009, when a cold front caused the collapse of the Puerto Colombia pier [46]. The water quality in the MRE varies with climatic seasons. During the dry season occurs the highest average variability in the surface salinity (12.5 ± 3.3), the lowest average of chlorophyll-a concentration (1.6 mg m^{-3}), and the lowest average of surface temperature (24.1 ± 1.0 °C). The peak average surface temperature takes place in October (29.3 ± 1.0 °C), while the highest average concentration of chlorophyll-a is observed in December (4.3 mg m^{-3}). These characteristics classify the primary nutrient production between the oligo-mesotrophic state ($30 < TSI \leq 40$) and mesotrophic state ($40 < TSI \leq 50$) [47]. The heavy metal concentrations in the sediment display variations along the riverbed. In the MRE, the concentrations ($\mu\text{g/g}$) are as follows: Co 9.48, Ni 26.8, Cu 26.9, Zn 99.0, Cd 2.02, Hg 0.12, Pb 16.8. The elements Ni and Hg surpass the average value plus 1.5 standard deviations (Ni 17.0 and Hg 0.04), resulting in a high potential ecological risk [48,49]. The Caribbean coast of Colombia exhibits a mixed and semi-diurnal microtidal pattern, as indicated by the Courtier coefficient ($1.43 \leq F \leq 1.9$). Even during high tide, its tidal range does not exceed 70 cm in height [50–52]. The climate also shares a long-standing relationship with the El Niño Southern Oscillation (ENSO) in both of its phases, El Niño and La Niña. The ENSO warm phase (El Niño) is associated with decreased precipitation and lower sea levels, while the ENSO cold phase (La Niña) is linked to higher sea levels and excessive rainfall [53–55].

3. Methodology

The assessment of stratification and mixing patterns was conducted using a MOHID model that had been previously calibrated. This model considered multiple factors, including bathymetry, river discharge, waves, and tides, to simulate the estuary circulation as a function of the buoyancy gradient and bottom frictional stresses [29,30,34,56,57].

MOHID was developed by MARETEC, the Marine, Environment and Technology Center at the Technical University of Lisbon. It is a three-dimensional numerical model that simulates the response of water bodies to physical and biogeochemical processes, factoring in the interaction between water–atmosphere and water–sediments. MOHID was developed utilizing a block programming structure, which encompasses specialized modules to solve hydrodynamics, water quality, and particle tracking equations [58]. The MOHID hydrodynamic module resolves the formulations of motion for incompressible and hydrostatically balanced fluids using the finite volume method and the Boussinesq and

Reynolds approaches [59]. The system's horizontal discretization employs an Arakawa-C-type computational grid [60], while the vertical axis enables the combination of Cartesian, Sigma, and Lagrangian coordinates. An implicit alternating direction algorithm is utilized to solve these equations, calculating the change in water elevation and velocities [61,62]. The vertical turbulence is inferred using the k- ϵ General Ocean Turbulence Model (GOTM) with a Canuto closure scheme [63]. For the horizontal turbulence, the Smagorinsky approach was employed with a coefficient value of 0.1. The selection was made based on its closeness to the measured data for both the flow velocity and salinity (refer to Table 1). Finally, horizontal and vertical advection and the diffusion of momentum, heat, and mass were managed through the implementation of the total variation diminishing method (TDV).

A total of 26 scenarios were analyzed under varying flow rates and tide conditions along a 22.0 km cross-section of the channel. To simulate the driving mechanism of the tides, winds, and river flow, MOHID was implemented in a two-tiered nesting system (see Figure 1). The outer grid was configured to operate at a coarser resolution in barotropic mode with 220×250 nodes ($\Delta x = \Delta y = 160$ m and $\Delta t = 10$ s). The values for the bottom roughness and horizontal turbulence were established as 0.0025 m and $10 \text{ m}^2/\text{s}$, respectively. The inner grid was set to operate in baroclinic mode with 242×172 nodes operating at ($\Delta x = \Delta y = 80$ m and $\Delta t = 5$ s) with a vertical discretization of 48 layers using Cartesian coordinates. This configuration enabled the simulation of localized sub-regions, such as the salt wedge intrusion, while minimizing computational resource usage. The engaged flow rates ranged from 2000 to $6500 \text{ m}^3/\text{s}$. Tidal simulations were conducted during both spring and neap states, demonstrating consistent and high-quality results with skill scores ranging from 0.94 to 0.97 and negligible bias (less than 0.01 m). To measure the overall effects of tides on the salt wedge position, the water properties pertaining to salinity, density and velocity were averaged over two tidal cycles (25 h) at a one-hour resolution (Figure 2).

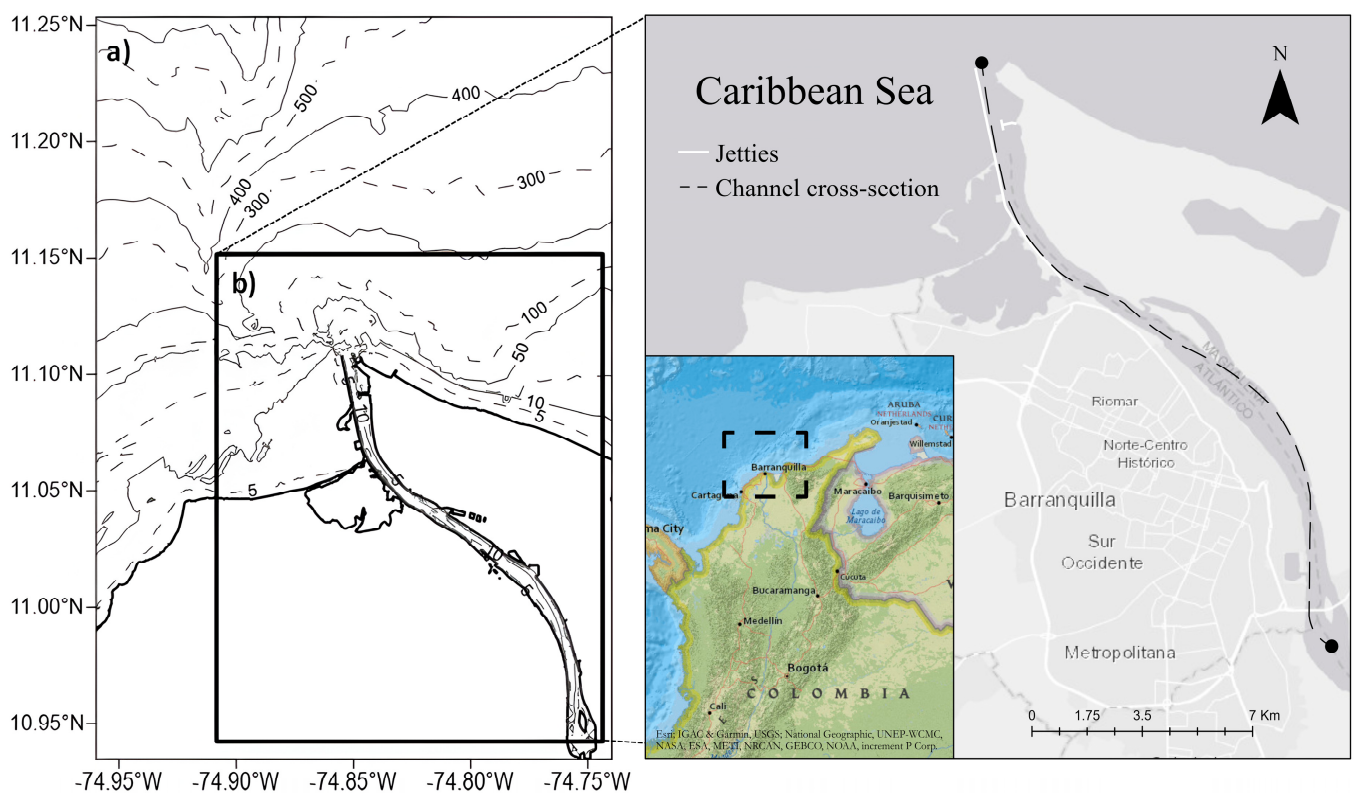


Figure 1. Location and computational domain of the MRE: (a) outer mesh; (b) detailed mesh.

Table 1. The bias, RMSE, and Willmott scores of the implemented MOHID model.

Feature	Bias	RMSE	Willmott	Source
Salinity	0.04 gr/kg	0.52 gr/kg	0.95	[30]
Velocity	0.0085 m/s	0.0034 m/s	0.7568	
Water level	<0.01 m	<0.01 m	0.91–0.96	
Potential energy anomaly	−0.05	6.2	0.99	[34]
Buoyancy frequency	−0.0477	0.00014	0.99	
Richardson number	−0.08	0.13	0.99	

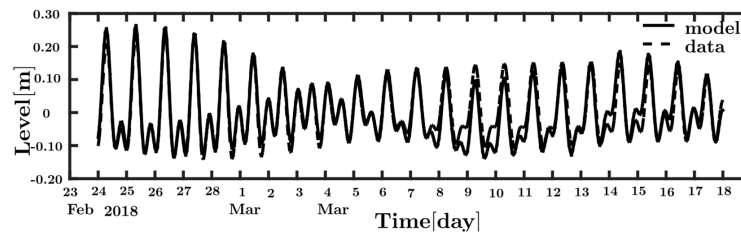


Figure 2. Water level series employed for spring and neap modeling scenarios.

This model was calibrated with field measurements showing reliable and practical depictions of the MRE. Table 1 compares the bias, RMSE, and Willmott coefficients [64] of the simulated and measured data for water salinity, velocity, and level during the dry season of February to March in 2018 and March 2020 [30]. The computed φ , β , and RL values were based on field measurements taken during March of 2014 [34].

3.1. Stratification and Mixing Parameters

To evaluate the strength of saline wedge stratification in every scenario, several physical parameters were calculated, including stratification (ϵ), buoyancy frequency (β), potential energy anomaly (φ), Richardson number by layer (RL), and turbulence production (P) (refer to Table 2).

Table 2. Stratification and mixing parameters.

Parameter Formulation	Meaning
Stratification $\left(\epsilon = \frac{\partial \rho}{\rho_0}\right)$	It is a dimensionless measurement of the stratification intensity based on the density of the water column. Here, the density gradient is represented by $\partial \rho = \rho(\text{bottom}) - \rho(\text{surface})$ and the average density is expressed as $\rho_0 = 0.5(\rho_b + \rho_s)$. Usually, this parameter reaches values between 0 (indicating a well-mixed water plot) and 0.025 (indicating a highly stratified water plot) [8].
Buoyancy Frequency $\left(N^2 = \beta = -\frac{g}{\rho} \frac{\partial \rho}{\partial z}\right)$	It is a cycle/s ² index of the oscillation frequency of a vertically displaced water plot ($\beta > 0$) while tending to balance hydrostatically. Here, g represents the gravity acceleration, $\partial z = z(\text{bottom}) - z(\text{surface})$ is the depth gradient, and $\partial \rho = \rho(\text{bottom}) - \rho(\text{surface})$ represents the density gradient. As β decreases, the consumption of kinetic energy involved in the production of turbulent mixing increases, resulting in a lower degree of stratification [65].
Potential Energy Anomaly $\left(\varphi = \frac{1}{h} \int_{-h}^0 (\bar{\rho} - \rho) g z \partial z\right)$	It evaluates the work per volume unit necessary to mix a water column. Here, $\bar{\rho}$ is defined as $\bar{\rho} = \frac{1}{h} \int_{-h}^0 \rho \partial z$, h is the water column depth, and z is the depth range. When a water column is fully salty or fresh, φ tends toward zero. Its unit are J/m [66].
Richardson Layered Number $\left(RL = \frac{g h (\rho_f - \rho_s)}{u^2 \rho_0}\right)$	It provides an estimate of the vertical mixture intensity by comparing the buoyant force and the shear stress. When $RL < 2$, the turbulence generated by friction is the main mixing mechanism. For $2 < RL < 20$, the mixture becomes less effective. $RL > 20$ indicates that the water plot is stable and homogeneous. It is dimensionless [67].
Turbulence Production * $\left(P \cong \frac{u^3}{kz}\right)$	This parameter assesses the production of bottom swirls because of the Reynolds stresses and the mean shear. Here, k is the Von Karman constant (0.41), z is the depth, $u^2 = C_d (u_1)^2$ is an alternative to expressing friction in terms of speed, and C_d is the drag coefficient. It is measured in W/Kg [68].

Note: * This is a turbulence production simplification for the bottom.

3.2. Definition of the Flow Scenarios

Acknowledging the pivotal role of the river outflow in the spatial position of the salt wedge [29,30], it is imperative to comprehend the seasonal probability distribution of this factor. Such comprehension will establish a connection between the numerical modeling results and flow rate regimes. Based on daily field measurements from a limnometric station located in the municipality of Calamar [69], the MR exhibits a strong monthly variability (see Table 3). Therefore, to assess its seasonal behavior, it was necessary to calculate the empirical cumulative distribution function (ECDF) [70]. This approach offers insights into the frequency and probability associated with each discharge magnitude.

Table 3. Mean monthly streamflow (Q), maximum streamflow (Q_{max}), minimum streamflow (Q_{min}) and discharge variability (Q_{max}/Q_{min}) in the Magdalena River per month. Data interval: 23 July 1940 to 31 December 2015.

Month	Q (m ³ /s)	Q _{min} (m ³ /s)	Q _{max} (m ³ /s)	Q _{max} /Q _{min} (m ³ /s)
January	6822	2326	13,844	5.95
February	4474	1705	10,074	5.91
March	4129	1520	8434	5.55
April	4938	2053	9951	4.85
May	6854	3402	12,892	3.79
June	8153	4667	14,475	3.10
July	7874	3132	14,425	4.61
August	7284	3109	13,063	4.20
September	7464	3214	13,196	4.11
October	8443	3699	13,920	3.76
November	9806	4594	16,913	3.68
December	9724	2916	16,913	5.80

The ECDF is a non-parametric estimator of the cumulative distribution function (CDF) based on the frequency of a given flow (x) relative to the total number of observations (n). It is a step function that only takes values in the range from 0 to 1 and indicates the fraction of the data that is less than or equal to x [71]. The ECDF was applied to each series of daily flows per month, and then grouped by climatic stations (see Figure 3).

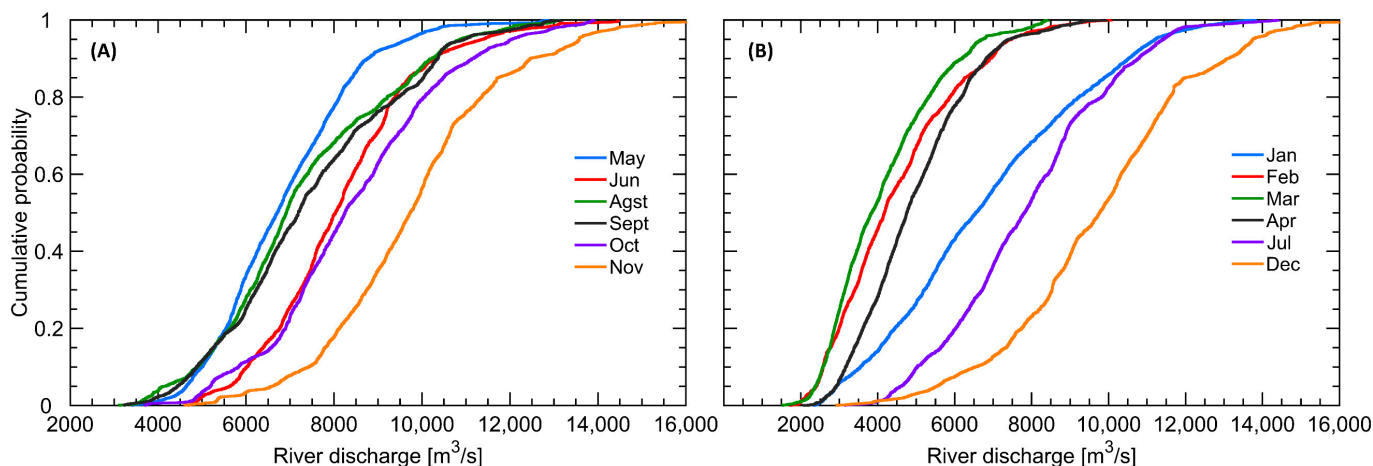


Figure 3. Average flow regime at the estuary of the Magdalena River: (A) during wet season; (B) during dry season.

4. Results

4.1. Average Monthly Flow Rate

The wet season includes the months related to the period of weak winds and high rainfall over the Colombian Caribbean. During this period, the flow of the MR reaches its

highest levels of the year ($\sim 16,900 \text{ m}^3/\text{s}$). This is the opposite of the dry season, when the trade winds strengthen, bringing dry air from the Atlantic Ocean to the Caribbean. This event causes a decrease in the frequency and amount of precipitation, causing daily flows in the order of $\sim 2500 \text{ m}^3/\text{s}$.

During the transition from the wet to the dry season, the variability in flow reaches its peak in January and maintains a high level ($Q_{\max}/Q_{\min} = 5.91$) until February (refer to Table 3). This phenomenon is primarily due to the absence of rainfall between February and March at the river's estuary, coinciding with the Magdalena River basin's flushing and the ITCZ positioning. It is evident that during these months, the probability distribution curve can be segmented into two distinct phases (see Figure 3B). An initial period of low slope and greater variability with flows between 4000 and 10,000 m^3/s achieved 50% of the time, followed by another high-slope phase with discharges between 1500 and 4000 m^3/s . This pattern confirms that the influence of the rainfall regime does not occur simultaneously.

Table 4 displays the accumulated probability of flows ranging from 2000 to 6500 m^3/s . The table is sectioned into 500 m^3/s increments, and the months with the greatest cumulative probability for each interval are outlined.

Table 4. Monthly cumulative probabilities for flows between 2000 and 6500 m^3/s .

Flow Rate (m^3/s)	Months with the Highest Probability of Occurrence	P. Accumulated (%)
$2000 \leq Q \leq 2500$	February and March	7.2 and 7.7
$2500 < Q \leq 3000$	February and March	12.9 and 16.7
$3000 < Q \leq 3500$	February, March, and April	12.0, 16.7, and 10.7
$3500 < Q \leq 4000$	February, March, and April	13.7, 11.9, and 11.0
$4000 < Q \leq 4500$	February, March, and April	11.0, 11.7, and 14.3
$4500 < Q \leq 5000$	February, March, April, May, and September	10.1, 10.1, 13.4, 6.6, and 6.3
$5000 < Q \leq 5500$	February, March, April, May, August, and September	8.4, 7.8, 11.5, 9.5, and 6.5
$5500 < Q \leq 6000$	January, April, May, August, and September	8.2, 10.4, 14.4, 10.1, and 6.9
$6000 < Q \leq 6500$	January, April, May, June, July, August, and September	7.0, 8.2, 11.9, 7.3, 7.6, 11.2, and 10.7
$Q > 6500$	January, May, June, July, August, September, October, November, and December	50.5, 54.3, 82.9, 72.6, 60.7, 64.1, 85.7, 95.5, and 90.1

It is worth noting that flows ranging from 2000 to 3000 m^3/s are considered uncommon occurrences. Even in March, the month with the highest likelihood of these ranges, their total magnitude does not exceed 24.31%. On the other hand, flows beyond 6500 m^3/s occur 90.12% of the time in December, 95.48% in November, and 85.65% in October. During the wet season, only scenarios with high flows have practical likelihoods. Conversely, in the dry season, there is more variability in flows that fall below 6500 m^3/s . For instance, in February and March, flows ranging from 2000 to 5500 m^3/s have a cumulative probability of 75.3% and 82.6%, respectively. These findings offer insight into the correlation between months when turbulent mixing is expected to decrease or increase based on the river's seasonal flow.

4.2. Tidal Effects on the Stratification and Penetration of the Salt Wedge

Figures 4 and 5 depict the stratification parameters, buoyancy frequency, potential energy anomaly, and bottom turbulent kinetic energy production for the defined flow scenarios. In general, the vertical structure of the halocline and pycnocline follows a consistent pattern across tidal cycles, with notable variations for flows ranging from 5000 to 6500 m^3/s . At syzygy tides, the stratification indices exceed 0.023 within the range of km 0 to 0.321 of the estuary. However, during the quadrature phase, only flows of 5000 and 5500 m^3/s exhibit a value of $\epsilon \geq 0.0226$ between km 0 and 0.562. For flows of 6000 and 6500 m^3/s , the stratification index is less than 0.083 in the distance interval between 0 and 0.562 km. This indicates that tidal waves have a stronger impact on the vertical stratification when the flow exceeds 5000 m^3/s .

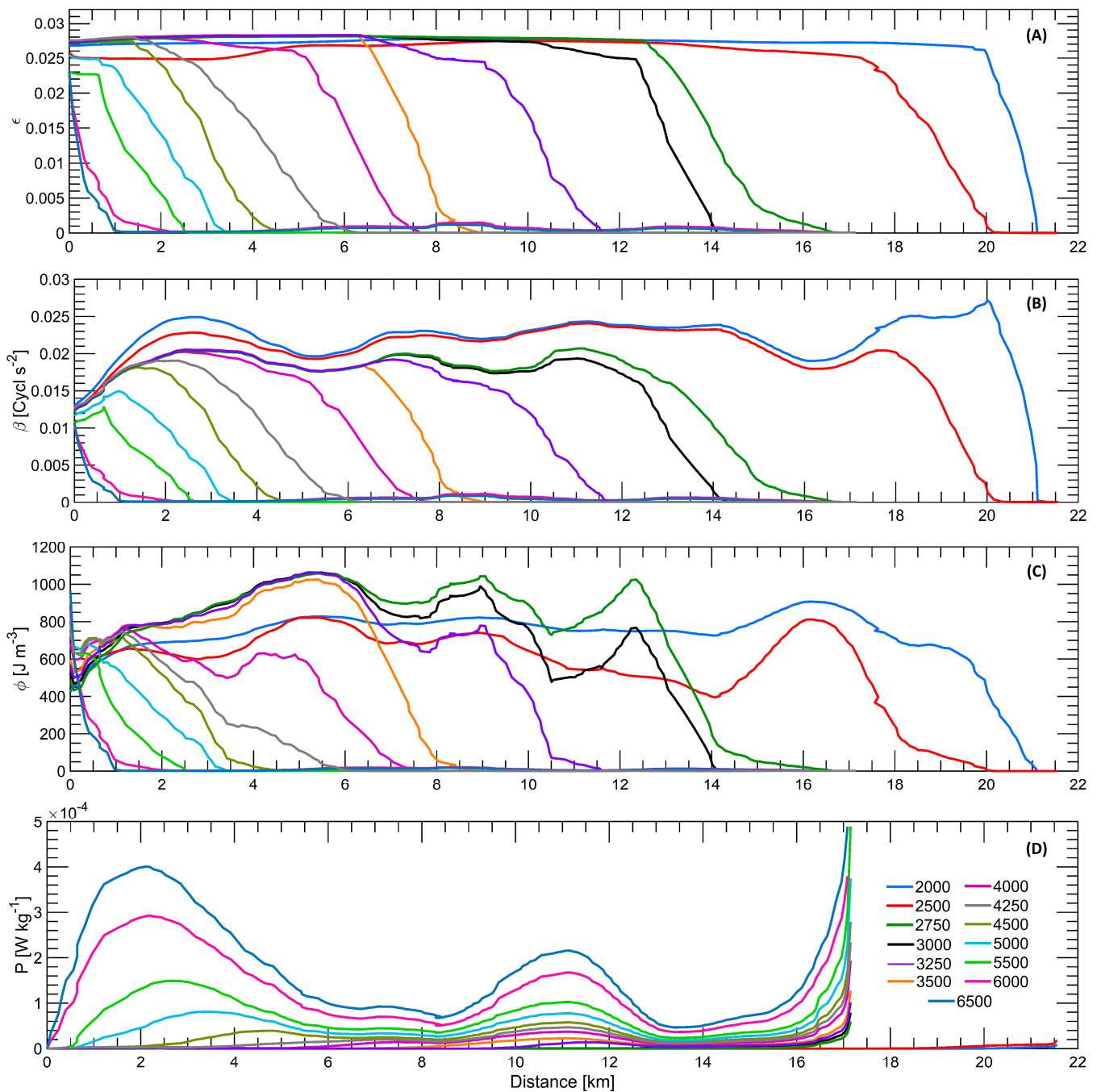


Figure 4. Physical parameters during quadrature tides: (A) stratification; (B) buoyancy frequency; (C) potential energy anomaly; (D) bottom turbulent energy production.

This is supported by analyzing the buoyancy coefficients and potential energy anomaly. Various methods are used to measure the degree of stratification in an estuary. Buoyancy refers to the inclination of a water column to rise or fall compared to an adjacent column due to differences in density, while the potential energy anomaly is the amount of energy required to mix a water column compared to the amount of energy required to mix the same quantity of water in a homogeneous column. Therefore, both indicators approach zero as the stratification intensity decreases. Additionally, it should be noted that within the flow range of 5000 to 6500 m³/s, the buoyancy and potential energy anomaly reach their maximum values, albeit of lesser magnitude during quadrature as compared to syzygy. Moreover, it has been confirmed that the attenuation of these parameters is higher when

the discharge values are 6000 and 6500 m³/s. For instance, at a distance of 560 m inland, buoyancy changes from having a maximum value of $\beta = 0.0132 \text{ s}^{-2}$ during syzygy to a value of $\beta = 0.0042 \text{ s}^{-2}$ in quadrature. This finding establishes that the salt wedge's response to tidal cycles is not only apparent when the river flow surpasses 5000 m³/s, but it is also magnified between 6000 and 6500 m³/s. Furthermore, it has been discovered that the tide has an impact on the maximum intrusion penetration, causing differences of up to 1000 m. The most significant variations occur during discharges of 2500, 3500, 4250, 4500, 5500 m and 6500 m³/s.

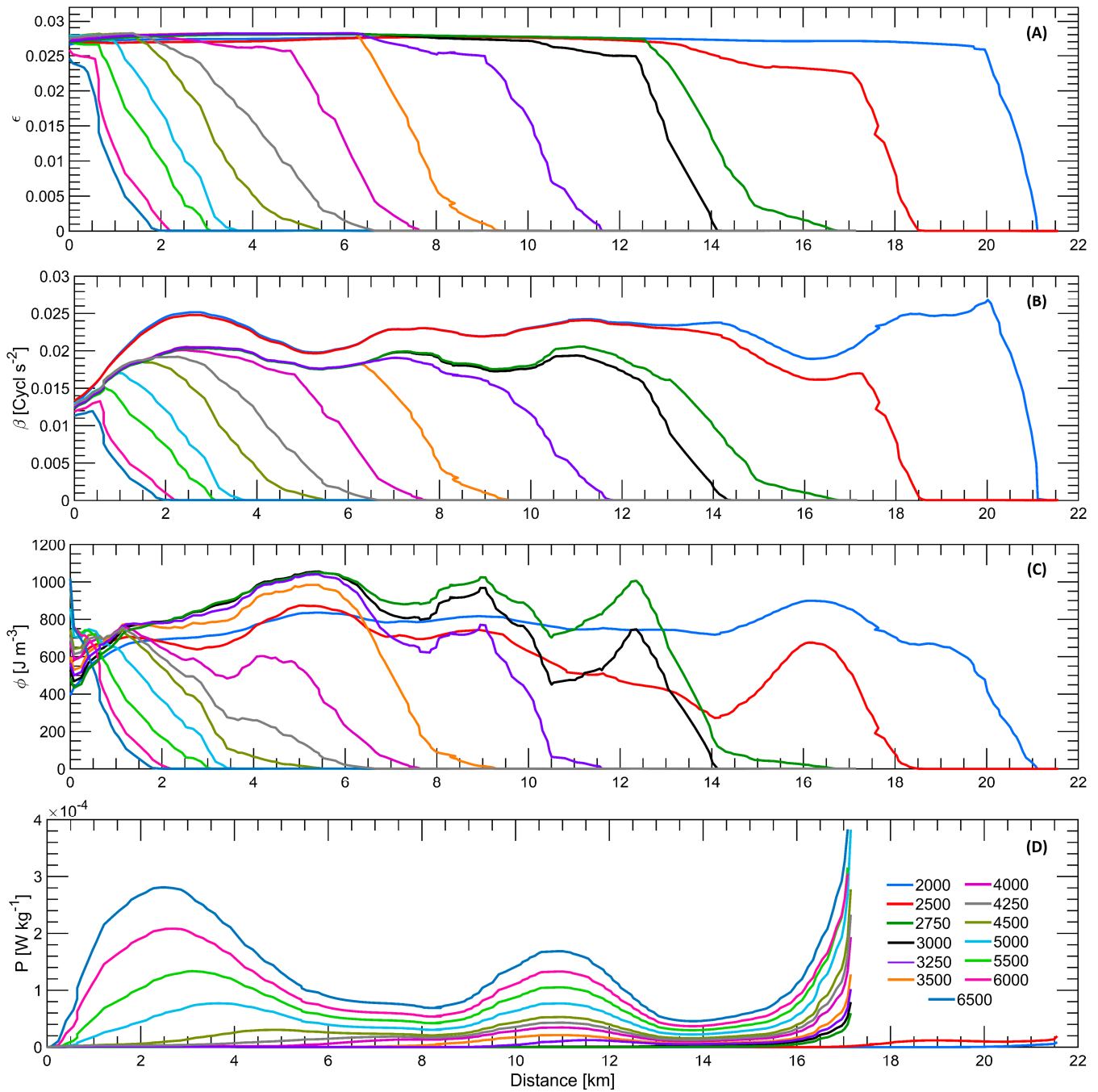


Figure 5. Physical parameters during syzygy tides: (A) stratification; (B) buoyancy frequency; (C) potential energy anomaly; (D) bottom turbulent energy production.

Richardson number (as shown in Figures 6 and 7) and bottom turbulent energy production (as seen in Figures 4D and 5D) are key indicators for assessing flow dynamics in relation to the stratification degree of the water column. The Richardson number reports that the fluid can maintain its stratification despite turbulent motions, while turbulent energy production signifies the amount of kinetic energy released into the water during turbulence. It has been observed that the maximum turbulence magnitudes are lower during syzygy tides along the entire section compared to those in quadrature. However, at low flow rates, the stability of the Richardson number remains coherent. As the flow rate intensifies, the bottom turbulence increases and causes mixing, thereby reducing the stability of the water parcel. As the flow rate increases, it is argued that its ability to mix and hold particles in suspension also increases, thus limiting the precipitation of flocules.

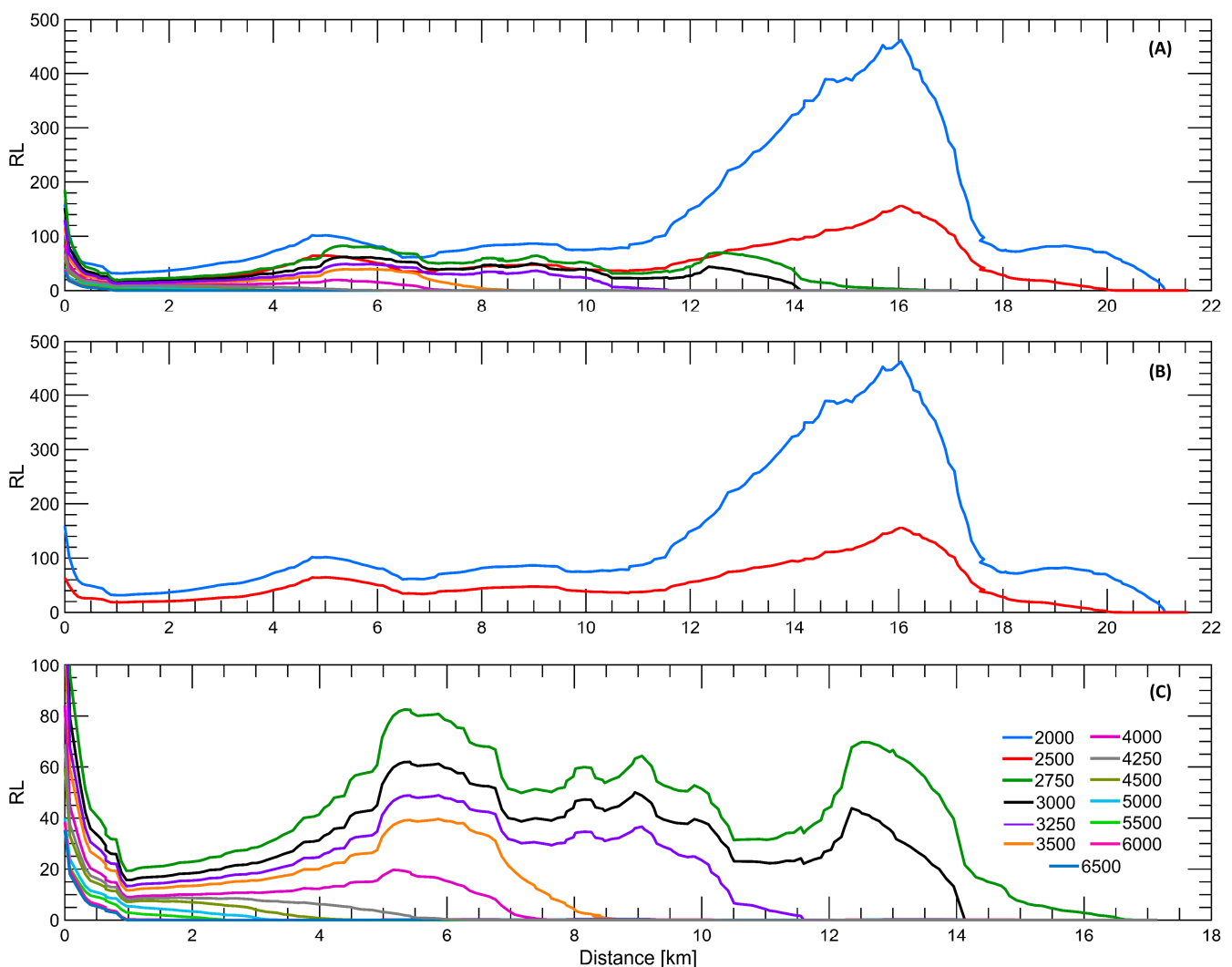


Figure 6. Richardson by layers (RL) at quadrature tide in: (A) all flow scenarios; (B) only the flow rates between 2000 and 2500 m^3/s ; (C) the flow rates ranging from 2750 to 6500 m^3/s .

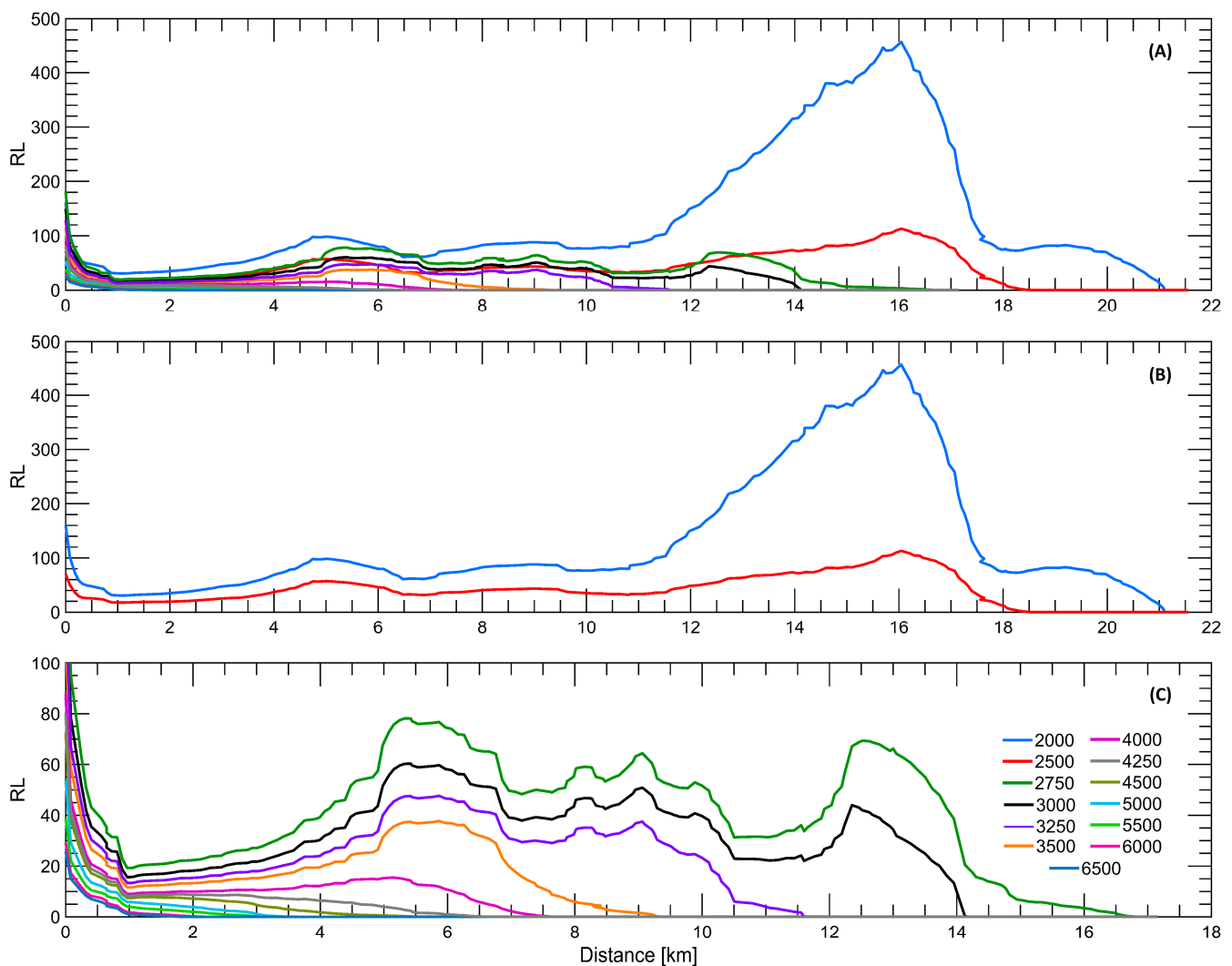


Figure 7. Richardson by layers (RL) during syzygy tides in: (A) all flow scenarios; (B) only the flow rates between 2000 and 2500 m^3/s ; (C) the flow rates ranging from 2750 to 6500 m^3/s .

4.3. Effects of Flow Rate on FSI Position

According to [31], the location of the TMZ core is associated with the position of the freshwater–saltwater interface (FSI). The maximum depth of the FSI is recognized by the decrease in salinity and longitudinal density in the water column to its minimum, which is easily distinguishable in all stratification parameters.

FSI for Flow Rates from 2000 to 3000 m^3/s

In this flow range, the FSI lies between km 14.3 and 21 of the section. There are distinct stratification levels between km 0 and 12, which are longitudinally maintained ($\epsilon \sim 0.026$ and $\beta \sim 0.019 s^{-2}$). Upstream, the gradual increase in mixing in the water column causes all parameters to decrease to their minimum values. At $Q = 2000 m^3/s$, this happens from kilometer 20, while at $Q = 3000 m^3/s$, it occurs from kilometer 12. For $Q = 2500 m^3/s$, the location depends on the tidal stage: it happens at kilometer 17 during syzygy and at kilometer 17.5 during quadrature. The turbulent energy production at the riverbed is negligible ($P \sim 0 W/Kg$), resulting in underdeveloped mixing along the DDRM. In other words, greater levels of frictional strain are required to disrupt the stratification. This is confirmed by the Richardson number behavior ($RL > 20$), which results in a stable column (stratified) due to the dominant buoyant force on the turbulent bottom currents. At flow rates of $Q = 2000$ and $2500 m^3/s$, the stability greatly increases ($RL \gg 20$) within the range

of approximately km ~11.5 to ~17.5 due to the channel's lateral widening. For a flow rate of $Q = 2750$ and $3000 \text{ m}^3/\text{s}$, the potential energy anomaly φ concentrates energy in three locations where the maximum work required for water mixing is at approximately ~5.5, ~9, and ~12.5 km. This is followed by two valleys at approximately ~7.5 and ~10.5 km. All locations have values of $\varphi > 470 \text{ J/m}^3$, which reaffirms the intense degree of stratification.

FSI for Flow Rates from 3250 to 4000 m³/s

The FSI spans from km 7.6 to 11.7. Throughout the initial section (km 0–km 5), the indicators $\epsilon \sim 0.0275$ and $\beta \sim 0.0185 \text{ s}^{-2}$ remain substantially unchanging. However, the stratification weakens beyond km 5 for $Q = 4000 \text{ m}^3/\text{s}$, km 6 ($Q = 3500 \text{ m}^3/\text{s}$), and km 9 ($Q = 3250 \text{ m}^3/\text{s}$) due to the increasing bottom turbulent production. At $Q = 4000 \text{ m}^3/\text{s}$ (located between km 6 and 13), the production is at $\sim 3.45 \times 10^{-5} \text{ W/Kg}$. At $Q = 3500 \text{ m}^3/\text{s}$ (located between km 9 and 13), the production is at $P \sim 2.11 \times 10^{-5} \text{ W/Kg}$. Lastly, at $Q = 3250 \text{ m}^3/\text{s}$ (located between km 10 and 13), it is the same as $2.11 \times 10^{-5} \text{ W/Kg}$. The stability of the column, as anticipated, undergoes a decline when it is at $Q = 4000 \text{ m}^3/\text{s}$, whereby turbulent kinetic energy has a similar magnitude to hydrostatic potential energy. Specifically, RL acquires values between 2 and 20 explaining, the weakening of the salt layering by the mixing strengthening. At $Q = 3250 \text{ m}^3/\text{s}$, the φ index initially rises from 565 J/m^3 at km 0 to 1040.6 J/m^3 at 5.4 km but subsequently declines as the stratification intensity increases.

FSI for Flow Rates from 4250 to 6500 m³/s

The FSI is between kilometers 1 and 6.5. Regarding the parameters, it is observed that at $Q = 4250 \text{ m}^3/\text{s}$, the maximum value of bottom turbulence is $4.30 \times 10^{-5} \text{ W/Kg}$ at km 11. At $Q = 4500 \text{ m}^3/\text{s}$, the maximum turbulence (P_{max}) is $5.29 \times 10^{-5} \text{ W/Kg}$ and is also achieved at kilometer 11. At $Q = 5000 \text{ m}^3/\text{s}$, the turbulent production starts at km 1.2 and equals two peaks: $P_{max} = 7.706 \times 10^{-5} \text{ W/Kg}$ (3.6 km) and $P_{max} = 7.68 \times 10^{-5} \text{ W/Kg}$ (11 km). At $Q = 5500 \text{ m}^3/\text{s}$, β and φ suggest a decrease in stratification toward the Caribbean Sea during quadrature when comparing the maximum values in this phase ($\beta = 0.0128 \text{ s}^{-2}$) ($\varphi = 636.18 \text{ J/m}^3$) with the maximum values achieved during syzygy ($\beta = 0.0151 \text{ s}^{-2}$) ($\varphi = 754.55 \text{ J/m}^3$). For this flow rate, two peaks of turbulent production are reached: $P_{max} = 1.336 \times 10^{-4} \text{ W/Kg}$ (3.09 km) and $P_{max} = 1.05 \times 10^{-4} \text{ W/Kg}$ (11 km). At $Q = 6000 \text{ m}^3/\text{s}$, the stratification index decreases from 0.02 (immediately at the estuary) to 2.65×10^{-3} in the first kilometer and in the quadrature phase. In syzygy, this decrease begins 560 m later. Indeed, between 0 and 560 m, ϵ approaches 0.0245. A similar trend is seen for β and φ at km 1, $\beta = 0.0062 \text{ s}^{-2}$ (syzygy) and $\beta = 0.00145 \text{ s}^{-2}$ (quadrature), which ensures that at this distance, the tidal action has a stronger influence on the degree of stratification. In this scenario, mixing initiates at km 0 during quadrature, and km 0.25 in syzygy, which corresponds to two peaks of turbulent production. At $Q = 6500 \text{ m}^3/\text{s}$, the magnitude of turbulent production is even higher and starts from km zero with two peaks: $P_{max} = 2.08 \times 10^{-4} \text{ W/Kg}$ (2.68 km) and $P_{max} = 1.32 \times 10^{-4} \text{ W/Kg}$ (11 km), and $P_{max} = 2.80 \times 10^{-4} \text{ W/Kg}$ (2.52 km) and $P_{max} = 1.68 \times 10^{-4} \text{ W/Kg}$ (11 km).

5. Discussion

5.1. Tidal and Flow Effects on the Salt Wedge

The farthest extent reached by the parameters of stratification, buoyancy, and potential energy anomaly is interpreted as the upper limit of the influence zone of the saline wedge from three different perspectives. The first perspective simply relies on the calculation of the density gradient [72,73]. The second perspective explores the vertical stability between two layers of water with differing physical properties. The higher the buoyancy index, the greater the stability. Peak buoyancy values commonly occur within the pycnocline [74,75]. Lastly, the potential energy anomaly measures the mechanical energy needed to instantaneously homogenize a water column [76]. A comparative assessment of the maximum reach of the wedge under syzygy and quadrature tide conditions reveals the important influence of tides on the extent of saltwater ingress (Figure 8). The stratification index

indicates that during syzygy, there is a 1.5% increase in the depth of intrusion compared to quadrature. Likewise, the buoyancy frequency exhibits a parallel trend with a 1.42% increase. The potential energy anomaly reports a slightly higher total penetration of 2.6%. Nevertheless, this estimation may be imprecise when comparing stratification strengths at the same point during different tidal phases, particularly when the ratio of tidal amplitude to the thickness of the water column is not sufficiently small [77]. Within the $Q = 2000$ to $2500 \text{ m}^3/\text{s}$ range, the uppermost reach demonstrates a distinct pattern attributed to the widening of the channel geometry spanning kilometers 12 to 18. Despite this, all parameters consistently show an inversely proportional relationship between seawater infiltration and river discharge.

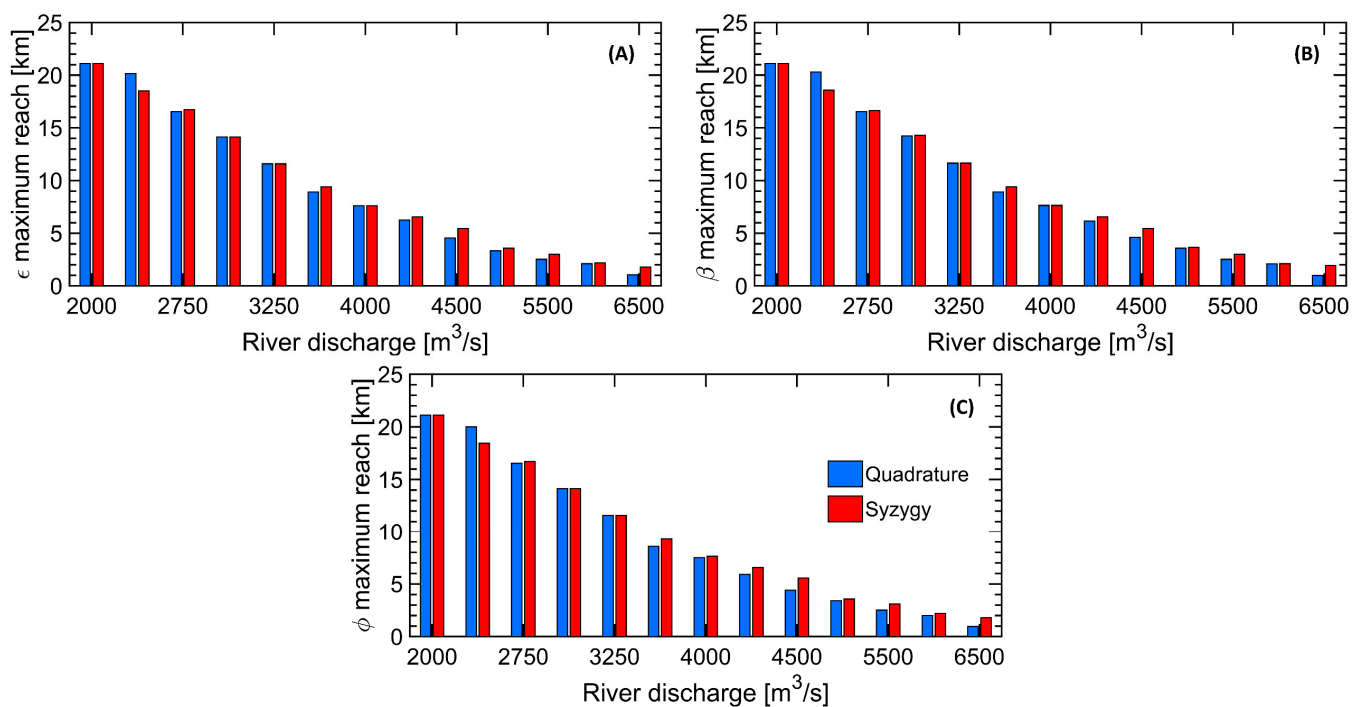


Figure 8. Tidal and flow comparison of the maximum reach of physical parameters: (A) stratification; (B) buoyancy frequency; (C) potential energy anomaly.

Based on the stratification and buoyancy parameters, it can be reaffirmed that the magnitude of flow rate and the FSI front displays a non-linear, inversely proportional relationship (as illustrated in Figure 9) described by the curve fitting formula $\text{FSI}(Q) = 1.133 \times 10^{-6} Q^2 - 0.0142 Q + 46.2825$. The given regression model has a coefficient of determination (R^2) of 0.9846, thereby reaffirming the river dominance in the MRE dynamics [29,30]. This model stands as a promising inaugural approximation for predicting the location of the FSI and, in extension, for delineating regions where the TMZ may consolidate [34]. Formerly, ref. [78] undertook this endeavor within the Pearl River estuary. This is a microtidal-fluvial estuary distinguished by its shallow depth and funnel-shaped geometry. They applied two regression methodologies, yielding results in alignment with our own findings. There is a non-linear, inversely proportional bond between the salt intrusion length and the river's hydrodynamics. Furthermore, estuarine salinity exhibits variability not only due to the primary influence of the river but also in connection with the temporal alignment of peak flow events relative to the baseline flow conditions. These patterns have been observed in numerous estuaries worldwide, primarily through the application of Van der Burgh's coefficients [79–81].

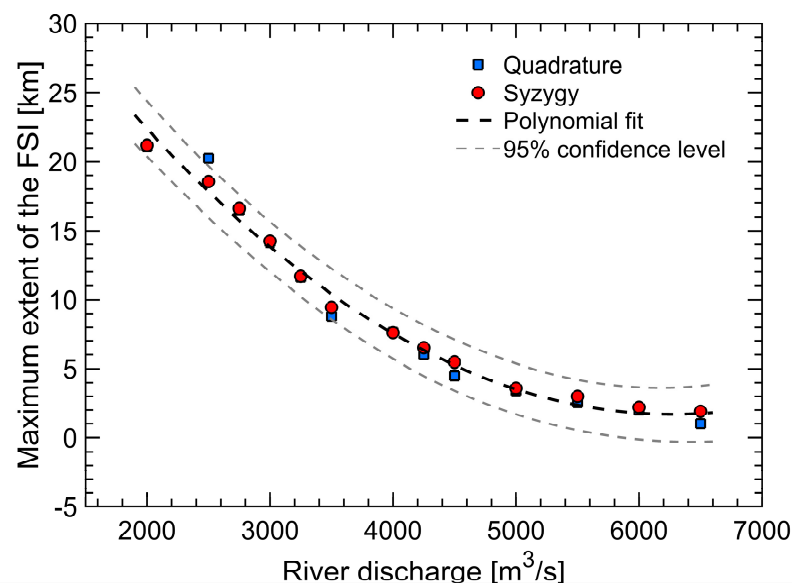


Figure 9. Position of FSI in relation to the flow of the Magdalena River. Fitting formula: $FSI(Q) = 1.133 \times 10^{-6} Q^2 - 0.0142 Q + 46.2825$ with a $R^2 = 0.9846$.

It is essential to recognize the limitations of this statistical fitting due to the role of tides in stratification and mixing in estuaries. Examining the same flow scenario, spring tides enhance salt layering. In contrast, during quadrature tides, mixing is increased, which implies less differentiation of layers in the water column. Based on the average impact of two tidal cycles, it was discovered that the intrusion depth can differ by up to 1 km. However, if morphological changes in the channel are considered, this variation could amplify exponentially. In the Guadalquivir River estuary, an escalation in tidal inflow was observed following bed-dredging operations [82]. In the Ems estuary, the deepening of the channel has led to heightened turbidity and sedimentation levels [83]. The rising sea level acts as another factor contributing to the variability in tide influxes [84,85]. In most scenarios, it results in an augmentation in both the length and volume of salt wedge intrusion [86,87]. These discoveries open up new avenues of study within the dredging context of the MR [27], encompassing short-term analyses throughout a complete tidal cycle.

The characteristics of the TMZ are determined by a composite interplay of channel morphology, sediment properties, river outflow, sea inflow, and other hydrodynamic processes. Typically, the TMZ tends to be situated in close proximity to the landward extremity of the salt wedge, and is assembled by near-bottom density gradients [88–90]. In the MRE, the core of the TMZ is not only downstream of the FSI, but usually remains in close proximity to it, regardless of flow or tidal phase [31]. This finding implies that the TMZ also experiences migration. Additionally, it was observed that TMZ intensifies with flocculation when the FSI penetrates into the countercurrent [34]. The flocculation capability of the TMZ is a result of the convergent shear fluxes within its boundaries [91]. The flocs emerge as a consequence of the aggregation of colloidal particles [92]. Their dimensions are subject to sediment availability, organic matter concentration, as well as advection and convection velocities [93–95]. In the MRE, a significant amount of organic and inorganic material is present in suspension [33]. Consequently, the flocculation process is mainly conditioned by the frictional stresses in the bed, which depend mainly on the MR. The discovery of this research indicates that the bottom turbulence production (P) and the Richardson number (RL) can be used to infer the magnitude of the shear stress at the bottom (τ_{xy}) given that P and τ_{xy} are directly proportional to each other, whereas RL and τ_{xy} are inversely related. The highest shear stresses occur between kilometers 0–6 and 9–13, and are greater when the river flow increases. Under quadrature tide conditions,

turbulent production averages 14.2% higher than during syzygy. In discharges ranging from 2000 to 4000 m³/s, the average water column stability increases by approximately 5.30% compared to syzygy. These enhancements are attributed to the FSI front position, and the ability of tides to counteract shear stresses at the river bottom, with a greater impact observed in low-flow scenarios. Deeper and more intense ebb and flow tidal currents lead to a reduction in bottom turbulence. Simultaneously, the increased tidal currents promote the vertical mixing of water parcels. Nevertheless, the primary factor conditioning water stability and bottom turbulent production remains the river (Figure 10).

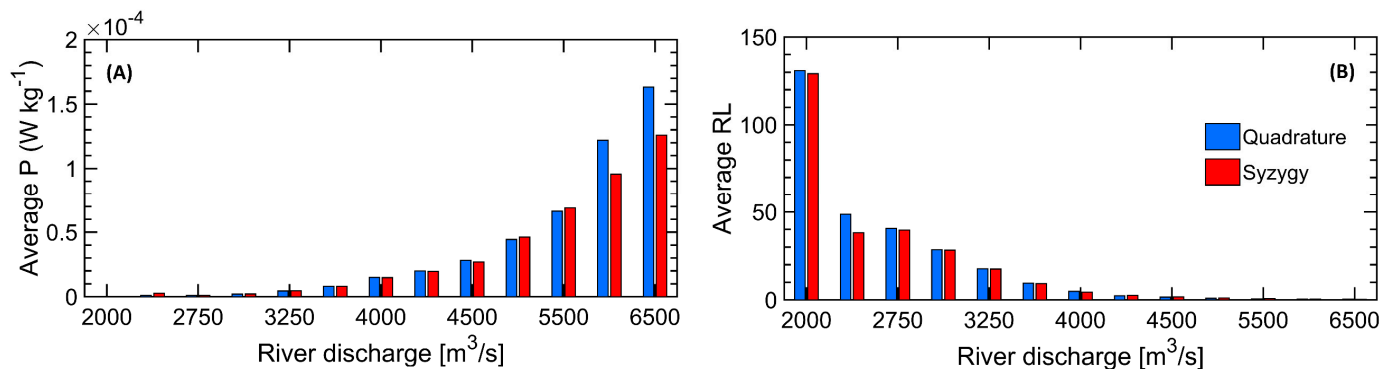


Figure 10. Tidal and flow comparison of the average magnitude of physical parameters: (A) bottom turbulent energy production; (B) Richardson number by layers.

Estuaries can be classified as partially mixed and salt wedge types based on their buoyancy coefficients (β). Partially mixed estuaries exhibit a β between 0.0025 and 0.01 s⁻², while salt wedge estuaries have β values between 0.01 and 0.1 s⁻² [65]. The findings obtained in this research confirm that the MRE can be classified into both categories depending on its tidal phase. During quadrature and syzygy, it behaves as a wedge estuary for flows below 5500 and 6500 m³/s, respectively. This implies that for flows above these limits, its theoretical configuration corresponds to that of a partially mixed estuary. According to [34], this limit is set at 4000 m³/s, regardless of the tidal cycle.

5.2. FSI Monthly Mobility

Although the Magdalena River can reach flows as high as 17,000 m³/s, analyzing its response to discharges below 6500 m³/s supplies sufficient insight into the dynamics of the salt wedge. It should be noted that it is in the lower-flow scenarios that the greatest variability in the magnitude of the FSI occurs.

Table 5 is created by integrating the stratification-mixing indicators in the estuary with a statistical analysis of flow regimes. It displays the monthly ranges where the FSI and TMZ are mobilized by proximity. For all instances, the cumulative probability (Pa) helps to validate the feasibility of each interval in both neap tide (NT) and spring tide (ST). In this sense, it can be stated that 90.1% of the time, flows between 6000 and 14,583 m³/s occur in December, which means that the FSI is unable to penetrate beyond 2.2 km, regardless of the tidal cycle. During this month, its lowest intrusion depth is estimated, and the highest turbulent production rate at the bottom of the estuary. As for January, the MR begins to decline, which results in a greater stratification and deepening of the saline wedge up to a maximum of 14.2 km. Approximately, this should be located around km 7.1 ± 7.1.

During February, the saline front gradually moves upstream, from oscillating around km 9.7 ± 9.7 to stopping above km 11 ± 10 in March, at which point it is expected to reach its maximum extent before receding due to increased river flow. By April, it is found above km 9.7 ± 9.7, above km 4.5 ± 4.5 in May, and at 1.8 ± 1.8 km in June. It advances against the current again for both July and August, stopping in both cases near km 5.8 ± 5.8. In September, the halocline is located at approximately km 4.5 ± 4.5 and retreats in October (km 1.8 ± 1.8), November (km 1.4 ± 1.4), and December (km 1.2 ± 1). This pattern

suggests that the FSI positioning is highly responsive to changes in intra-annual scales and consistently remains focused around km 5.

Table 5. Monthly FSI position during neap tide (NT) and spring tide (ST).

Month	Flow Rate (m ³ /s)	P. Accumulated (%)	NT-FSI	ST-FSI
December	6000–14,583	90.1	km < 2	km < 2.2
January	3000–11,428	90.0	km < 14.2	km < 14.2
February	2500–8350	90.2	km < 20.2	km < 18.5
March	2000–6500	92.2	km 1 and 21.1	km 1.9 and 21.2
April	2500–6976	90.6	km < 20.2	km < 18.5
May	3500–8823	90.1	km < 8.8	km < 9.4
June	5000–10,909	91.0	km < 3.4	km < 3.6
July	3250–10,909	91.0	km < 11.6	km < 11.6
August	3250–10,243	90.0	km < 11.6	km < 11.6
September	3500–10,380	90.0	km < 8.8	km < 9.4
October	5000–11,875	90.3	km < 3.4	km < 3.6
November	5500–13,215	90.3	km < 2.5	km < 3

Considering that accelerated floc precipitation occurs when turbulent stratification is disrupted, it can be argued that an increase in bed sedimentation is promoted during the initial phase of the dry–rainy climate transition. Two important processes take place during this phase. First, the capacity of the river to transport larger fragments increases. Second, the FSI–TMZ emerges from the stream, which favors sediment uptake. Specifically, it follows that during the most intense transition of the year (February–March–April), the precipitation volume peaks between km 1 and 9.7 ± 9.7 . Furthermore, it is expected that the periods of greatest erosion are associated with the restriction of the wedge above km 2, due to the increase in Q and the intensification of bottom shear.

5.3. Probabilistic Model Validation

Although the FSI–TMZ relationship proposed here is based on the characterization of the MR regime and the application of a previously calibrated and validated numerical model, it is evident that estuarine circulation processes involve complex interactions that are difficult to synthesize using such approaches [7]. For this reason, a case study is presented that integrates the probabilistic flow regime (refer to Figure 11) and a multi-bathymetric analysis of the bed for the year 2016.

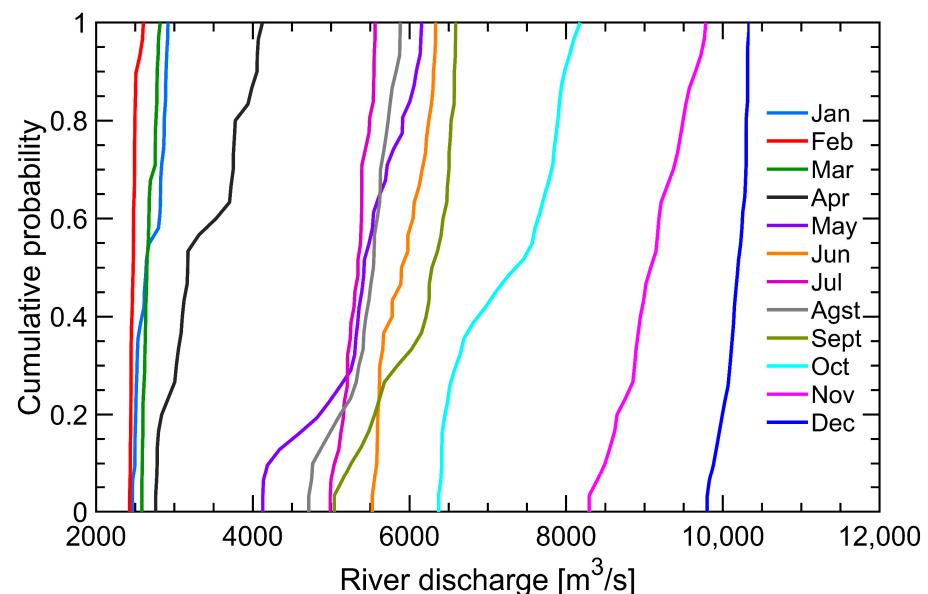


Figure 11. Monthly ECDF of flows for the year 2016.

Ref. [20] found that sedimentation processes were dominant during the transitions from March–February and August–July, with an average rate of 883 mm/m (March–February) and 271 mm/m (August–July). Moreover, the data collected showed that a maximum accumulation of 8628 mm/m was recorded above kilometer 4.5 in the August–July transition period. Similarly, the study discovered that the erosion processes with the highest intensity take place during the transitions of February–January, September–August, October–September, November–October, and December–November, as well as in close proximity to kilometer 4.5. The average scour rate ranged from 194 mm/m (October–September) to 952 mm/m (February–January) with a maximum of 13,222 mm/m in December–November. In April–March, May–April, June–May, and July–June, a mixed range was identified with a slight predominance of erosional processes. The range in average erosion and accommodation rates is 112–835 mm/m and 165–833 mm/m, respectively. However, there are spatial differences in the distribution of these processes. For instance, the most significant sedimentation processes occur between km 0 and 2 from June to May. In May–April, sedimentation arises on the western margin between kilometers 0 and 3. In July–June, it occurs on the eastern margin between km 0 and 3, and extending up to km 5 in April–March.

In line with the functional model presented in this research (refer to Table 6), the salt wedge can migrate up to a maximum of 20.2 km and 5.5 km in March–February and August–July, respectively. During the first period, there was a retreat observed from ~20 km (February) to ~17.5 km (March). This movement occurred due to a rise in mean flow magnitude of 200 m³/s (February: 2467 m³/s, March: 2681 m³/s) that resulted in the accumulation of particulate material without disrupting channel stratification. During the second period, there is a comparable occurrence where the average flow increases from 5268 m³/s (July) to 5323 m³/s (August) with a maximum amplitude of 3.6 km (July) and 5.5 km (August). Note that the average sedimentation rate in March–February is more than three times higher than in August–July, and that turbulent energy production is practically nil for flows between 2500 and 3000 m³/s (March–February). This is different from the production related to discharges in the order of 5000 m³/s (August–July), which has two energy maxima: at kilometer 3 ($P_{max} = 1.336 \times 10^{-4}$ W/Kg) and at kilometer 11 ($P_{max} = 1.05 \times 10^{-4}$ W/Kg). As mentioned, higher shear stresses on the bed promote resuspension and aggregation of material, while hindering its sedimentation. This is why the precipitated volume during March–February is much higher, and sedimentation in August–July is focused between kilometers 3 and 11. In this section, turbulent energy decreases substantially, which causes the deposition of the previously accreted flocs that remained in suspension (as seen in Figures 4D and 5D).

Table 6. Monthly FSI position during neap tide (NT) and spring tide (ST) in 2016.

Month	Flow Rate (m ³ /s)	P. Accumulated (%)	NT-FSI	ST-FSI
December	9800–10,334	93.7	km ~ 0	km ~ 0
January	2495–2917	88.9	km 20.2 and 14.2	km 18.5 and 14.2
February	2428–2507	89.6	km ~ 20.2	km ~ 18.5
March	2583–2780	90.3	km 20.2 and 16.5	km 18.5 and 16.6
April	2760–4054	90	km 16.5 and 7.6	km 16.6 and 7.6
May	4186–6155	90.3	km 6 and 2	km 6.5 and 2.2
June	5525–6306	90	km 2.5 and 1	km 3 and 1.9
July	4988–5548	90.3	km 3.4 and 2.5	km 3.6 and 3
August	4763–5884	90	km 4.5 and 2	km 5.5 and 2.2
September	5041–6573	90	km 3.4 and 1	km 3.6 and 1.9
October	6412–8177	90.3	km < 1	km < 1.9
November	8294–9650	90.0	km ~ 0	km ~ 0

During the analysis of intervals featuring the most significant erosion, it was found that a correlation exists with the periods when the wedge is constricted toward the river's estuary. Specifically, this correlation is noticeable at km 2.7 ± 0.8 in September and 3.5 ± 1.5 in August, and during the October–September period (km 1.4 ± 0.5 and km 2.5 ± 0.9),

November–October (km \sim 0 and km 1.4 ± 0.5), and December–November (km \sim 0). However, an anomaly occurs during the February–January period. Although the FSI–TMZ is capable of penetrating to a depth of approximately \sim 20.2 km, the river experiences a decrease in competence during this stage, with the mean flow dropping from 2706 m³/s to 2467 m³/s. As a result of this reduction in flow, suspended material is precipitated and moves toward the salt front.

6. Conclusions

Numerical modeling is a versatile and effective tool for predicting the behavior of the salt wedge in the Magdalena River under various scenarios. This facilitates the development of planning processes such as risk management, energy utilization of the saline gradient, and programming of dredging activities. Both the numerical model and the probabilistic scheme have proven to be valuable tools in the representation and prediction of stratification and estuarine mixing processes.

The findings of this research show the complex interconnection between river flow, the extent of intrusion, and the degree of salt wedge stratification. In particular, flow was identified as the main conditioning agent of the system. Therefore, the behavior of the MRE responds strongly to seasonal scales, as the flow is linked to the rainfall regime, and both the stratification and the horizontal extent of the FSI decrease as the water flow increases. Furthermore, the importance of tidal waves in the differentiation of layers and the degree of penetration of the FSI has been found. Significant variations of up to 1000 m have been observed in the extent and vertical structure configuration of the estuary, particularly during instances when river flow exceeds specific thresholds. These findings are crucial in comprehending the dynamics of the estuary involving sedimentation and bed erosion. In particular, it is noted that during the transitions between the dry and wet seasons, the volume of sediment deposited reaches its annual maximum. For most of the year, it is expected that the salt front will be located beyond kilometer 5, with a maximum range of 11 ± 10 km. However, the most significant erosion processes will likely occur between kilometers 3 and 11, during the months when the FSI is restricted to kilometer 2, leading to an increase in turbulent bottom production that limits floc settlement.

Finally, it is important to emphasize that the geometric configuration of the river plays a fundamental role in the stability of the water column. Indicators such as the Richardson number allow us to affirm that a widening of the channel strengthens the stability of the stratification in both syzygy and quadrature tides. In fact, the influence of this geometrical effect is stronger than the average variations between different tidal phases, as this parameter shows no significant changes between stages. This conclusion is particularly relevant to the dredging operations frequently undertaken in the Magdalena River estuary.

Author Contributions: Formal analysis, J.R.C.-A.; investigation, J.R.C.-A.; methodology, L.J.O.D.; software, A.E.H.Á.; supervision, L.J.O.D.; writing—original draft, J.R.C.-A.; writing—review and editing, L.J.O.D. and A.E.H.Á. All authors have read and agreed to the published version of the manuscript.

Funding: This research received no external funding.

Data Availability Statement: The numerical model data showcased in this study can be accessed in [30,34]. Discharge data for the Magdalena River are available in [69].

Conflicts of Interest: The authors declare no conflict of interest.

References

1. Pritchard, D.W. Estuarine circulation patterns. *Proc. Am. Soc. Civil Eng.* **1955**, *81*, 1–11.
2. Geyer, W.R.; MacCready, P. The Estuarine Circulation. *Annu. Rev. Fluid. Mech.* **2014**, *46*, 175–197. [[CrossRef](#)]
3. Valle-Levinson, A. 1.05-Classification of Estuarine Circulation. In *Treatise on Estuarine and Coastal Science*; Wolanski, E., McLusky, D., Eds.; Elsevier: Amsterdam, The Netherlands, 2011; pp. 75–86.
4. Haas, L.W. The effect of the spring-neap tidal cycle on the vertical salinity structure of the James, York and Rappahannock Rivers, Virginia, U.S.A. *Estuar. Coast. Mar. Sci.* **1977**, *5*, 485–496. [[CrossRef](#)]

5. Dyer, K.R.; New, A.L. Intermittency in Estuarine Mixing. In *Estuarine Variability*; Wolfe, D.A., Ed.; Academic Press: Cambridge, MA, USA, 1986; pp. 321–339.
6. Valle-Levinson, A. *Contemporary Issues in Estuarine Physics*; Valle-Levinson, A., Ed.; Cambridge University Press: Cambridge, UK, 2010.
7. MacCready, P.; Geyer, W.R. Advances in estuarine physics. *Annu. Rev. Mar. Sci.* **2010**, *2*, 35–58. [[CrossRef](#)] [[PubMed](#)]
8. Hansen, D.V.; Rattray, M., Jr. New Dimensions in Estuary Classification1. *Limnol. Oceanogr.* **1966**, *11*, 319–326. [[CrossRef](#)]
9. Perales-Valdivia, H.; Sanay-González, R.; Valle-Levinson, A. Effects of tides, wind and river discharge on the salt intrusion in a microtidal tropical estuary. *Reg. Stud. Mar. Sci.* **2018**, *24*, 400–410. [[CrossRef](#)]
10. Zachopoulos, K.; Kokkos, N.; Sylaios, G. Salt wedge intrusion modeling along the lower reaches of a Mediterranean river. *Reg. Stud. Mar. Sci.* **2020**, *39*, 101467. [[CrossRef](#)]
11. Couceiro, M.A.A.; Schettini, C.A.F.; Siegle, E. Modeling an arrested salt-wedge estuary subjected to variable river flow. *Reg. Stud. Mar. Sci.* **2021**, *47*, 101993. [[CrossRef](#)]
12. Krvavica, N.; Gotovac, H.; Lončar, G. Salt-wedge dynamics in microtidal Neretva River estuary. *Reg. Stud. Mar. Sci.* **2021**, *43*, 101713. [[CrossRef](#)]
13. Paiva, B.P.; Schettini, C.A.F. Circulation and transport processes in a tidally forced salt-wedge estuary: The São Francisco river estuary, Northeast Brazil. *Reg. Stud. Mar. Sci.* **2021**, *41*, 101602. [[CrossRef](#)]
14. Uncles, R.; Ong, J.; Gong, W. Observations and analysis of a stratification destratification event in a tropical estuary. *Estuar. Coast Shelf Sci.* **1990**, *31*, 651–665. [[CrossRef](#)]
15. Newton, A.; Icely, J.; Cristina, S.; Brito, A.; Cardoso, A.C.; Colijn, F.; Riva, S.D.; Gertz, F.; Hansen, J.W.; Holmer, M.; et al. An overview of ecological status, vulnerability and future perspectives of European large shallow, semi-enclosed coastal systems, lagoons and transitional waters. *Estuar. Coast. Shelf Sci.* **2014**, *140*, 95–122. [[CrossRef](#)]
16. Huang, P.; Kilminster, K.; Larsen, S.; Hipsey, M.R. Assessing artificial oxygenation in a riverine salt-wedge estuary with a three-dimensional finite-volume model. *Ecol. Eng.* **2018**, *118*, 111–125. [[CrossRef](#)]
17. Dyer, K. Estuarine Circulation. In *Encyclopedia of Ocean Sciences*; Steele, J.H., Ed.; Elsevier: Amsterdam, The Netherlands, 2001; pp. 846–852.
18. Guo, L.; He, Q. Freshwater flocculation of suspended sediments in the Yangtze River, China. *Ocean Dyn.* **2011**, *61*, 371–386. [[CrossRef](#)]
19. Silva-Dias, F.J.; Castro, B.M.; Lacerda, L.D.; Miranda, L.B.; Marins, R.V. Physical characteristics and discharges of suspended particulate matter at the continent-ocean interface in an estuary located in a semiarid region in northeastern Brazil. *Estuar. Coast. Shelf Sci.* **2016**, *180*, 258–274. [[CrossRef](#)]
20. Restrepo, J.C.; Orejarena-Rondón, A.; Consuegra, C.; Pérez, J.; Llinas, H.; Otero, L.; Álvarez, O. Siltation on a highly regulated estuarine system: The Magdalena River mouth case (Northwestern South America). *Estuar. Coast. Shelf Sci.* **2020**, *245*, 107020. [[CrossRef](#)]
21. Ming, Y.; Gao, L. Flocculation of suspended particles during estuarine mixing in the Changjiang estuary-East China Sea. *J. Mar. Syst.* **2022**, *233*, 103766. [[CrossRef](#)]
22. Geyer, W.R.; Woodruff, J.D.; Traykovski, P. Sediment Transport and Trapping in the Hudson River Estuary. *Estuaries* **2001**, *24*, 670–679. [[CrossRef](#)]
23. Li, M.; Ge, J.; Kappenberg, J.; Much, D.; Nino, O.; Chen, Z. Morphodynamic processes of the Elbe River estuary, Germany: The Coriolis effect, tidal asymmetry and human dredging. *Front. Earth Sci.* **2013**, *8*, 181–189. [[CrossRef](#)]
24. Orseau, S.; Huybrechts, N.; Tassi, P.; Van Bang, D.P.; Klein, F. Two-dimensional modeling of fine sediment transport with mixed sediment and consolidation: Application to the Gironde Estuary, France. *Int. J. Sediment Res.* **2021**, *36*, 736–746. [[CrossRef](#)]
25. Urbano Latorre, C.P.; Otero Díaz, L.J.; Lonin, S. Influencia de las corrientes en los campos de oleaje en el área de Bocas de Ceniza, Caribe Colombiano. *Boletín Científico CIOH* **2013**, *31*, 191–206. [[CrossRef](#)]
26. Assessment LC. 2.1.2 Colombia Port of Barranquilla [Internet]. 2021. Available online: <https://dlca.logcluster.org/212-colombia-port-barranquilla> (accessed on 18 December 2023).
27. MIN.TRANSPORTE. Cormagdalena y Findeter garantizan dragado en el río Magdalena en el 2021 gracias a la suscripción del contrato interadministrativo. Sitio web nacional Ministerio de Transporte Publicación [Internet]. 2020. Available online: <https://mintransporte.gov.co/publicaciones/9296/cormagdalena-y-findeter-garantizan-dragado-en-el-rio-magdalena-en-el-2021-gracias-a-la-suscripcion-del-contrato-interadministrativo/> (accessed on 18 December 2023).
28. Jang, D.; Hwang, J.H.; Park, Y.-G.; Park, S.-H. A study on salt wedge and River Plume in the Seom-Jin River and estuary. *KSCE J. Civ. Eng.* **2012**, *16*, 676–688. [[CrossRef](#)]
29. Ospino, S.; Restrepo, J.C.; Otero, L.; Pierini, J.; Alvarez-Silva, O. Saltwater intrusion into a river with high fluvial discharge: A microtidal estuary of the Magdalena River, Colombia. *J. Coast Res.* **2018**, *34*, 1273–1288.
30. Álvarez, A.H.; Otero, L.; Restrepo, J.C.; Álvarez, O. The effect of waves in hydrodynamics, stratification, and salt wedge intrusion in a microtidal estuary. *Front. Mar. Sci.* **2022**, *9*, 2296–7745.
31. Restrepo, J.C.; Schrottke, K.; Traini, C.; Bartholomae, A.; Ospino, S.; Ortíz, J.C.; Otero, L.; Orejarena, A. Estuarine and sediment dynamics in a microtidal tropical estuary of high fluvial discharge: Magdalena River (Colombia, South America). *Mar. Geol.* **2018**, *398*, 86–98. [[CrossRef](#)]

32. Arevalo, F.M.; Álvarez-Silva, Ó.; Caceres-Euse, A.; Cardona, Y. Mixing mechanisms at the strongly-stratified Magdalena River's estuary and plume. *Estuar. Coast. Shelf Sci.* **2022**, *277*, 108077. [[CrossRef](#)]
33. Restrepo, J.C.; Ospino, O.; Torregroza-Espinosa, A.C.; Ospino, S.; Villanueva, E.; Molano-Mendoza, J.C.; Consuegra, C.; Agrawal, Y.; Mikkelsen, O. Variability of suspended sediment properties in the saline front of the highly stratified Magdalena River estuary, Colombia. *J. Mar. Syst.* **2024**, *241*, 103894. [[CrossRef](#)]
34. Otero, L.J.; Hernandez, H.I.; Higgins, A.E.; Restrepo, J.C.; Álvarez, O.A. Interannual and seasonal variability of stratification and mixing in a high-discharge micro-tidal delta: Magdalena River, Colombia. *J. Mar. Syst.* **2021**, *224*, 103621. [[CrossRef](#)]
35. Álvarez, O.; Osorio, A. Salinity gradient energy potential in Colombia considering site specific constraints, Colombia. *Renew. Energy* **2015**, *74*, 737–748. [[CrossRef](#)]
36. Roldan-Carvajal, M.; Vallejo-Castaño, S.; Álvarez-Silva, O.; Bernal-García, S.; Arango-Aramburo, S.; Sánchez-Sáenz, C.I.; Osorio, A.F. Salinity gradient power by reverse electrodialysis: A multidisciplinary assessment in the Colombian context. *Desalination* **2021**, *503*, 114933. [[CrossRef](#)]
37. Sheppard, C. The Estuarine Ecosystem: Ecology, Threats and Management, Third Edition. *Mar. Pollut. Bull.* **2004**, *49*, 9–10. [[CrossRef](#)]
38. Statham, P.J. Nutrients in estuaries—An overview and the potential impacts of climate change. *Sci. Total Environ.* **2012**, *434*, 213–227. [[CrossRef](#)] [[PubMed](#)]
39. Torregroza, A.C. Spatio-temporal distribution of temperature, salinity, and suspended sediment on the deltaic front of the Magdalena River: Influence on nutrient concentration and primary productivity. *J. Artic. Salin. Mar. Sediments* **2020**, *24*, 10–120.
40. Higgins, A.; Restrepo, J.C.; Ortíz, J.; Pierini, J.; Otero, L. Suspended Sediment Transport in the Magdalena River (Colombia, South America): Hydrologic Regime, Rating Parameters and Effective Discharge Variability. *Int. J. Sediment Res.* **2015**, *31*, 25–35. [[CrossRef](#)]
41. Restrepo, J.C.; Ortíz, J.; Otero, L.; Ospino, S. Transporte de sedimentos en suspensión en los principales ríos del Caribe colombiano: Magnitud, tendencias y variabilidad. *Rev. Acad. Colomb. Cienc. Exactas Fis. Nat.* **2015**, *39*, 527–546. [[CrossRef](#)]
42. Milliman, J.; Farnsworth, K. *River Discharge to the Coastal Ocean: A Global Synthesis*; Cambridge University Press: Cambridge, UK, 2011.
43. Restrepo, J.C.; Schrottke, K.; Traini, C.; Ortíz, J.C.; Orejarena, A.; Otero, L.; Higgins, A.; Marriaga, L. Sediment Transport Regime and Geomorphological Change in a High Discharge Tropical Delta (Magdalena River, Colombia): Insights from a Period of Intense Change and Human Intervention (1990–2010). *J. Coast. Res.* **2015**, *32*, 575–589.
44. Pérez-Santos, I.; Schneider, W.; Sobarzo, M.; Montoya-Sánchez, R.; Valle-Levinson, A.; Garcés-Vargas, J. Surface wind variability and its implications for the Yucatan basin-Caribbean Sea dynamics. *J. Geophys. Res. Atmos.* **2010**, *115*, 10052. [[CrossRef](#)]
45. Ruiz, O.M. Variabilidad de la Cuenca Colombia (mar Caribe) Asociada con El Niño-Oscilación del Sur, Vientos Alisios y Procesos Locales. Departamento de Geociencias y Medio Ambiente, UNAL [Internet]. 2011. Available online: <https://repositorio.unal.edu.co/handle/unal/8181> (accessed on 18 December 2023).
46. Ortiz, J.; Otero, L.; Restrepo, J.C.; Ruiz, J.; Cadena, M. Characterization of cold fronts in the Colombian Caribbean and their relationship to extreme wave events. *Nat. Hazards Earth Syst. Sci.* **2013**, *13*, 2797–2804. [[CrossRef](#)]
47. Torregroza-Espinosa, A.C.; Restrepo, J.C.; Escobar, J.; Pierini, J.; Newton, A. Spatial and temporal variability of temperature, salinity and chlorophyll-a in the Magdalena River mouth, Caribbean Sea. *J. S. Am. Earth Sci.* **2021**, *105*, 102978. [[CrossRef](#)]
48. Tejeda-Benitez, L.; Flegal, R.; Odigie, K.; Olivero-Verbel, J. Pollution by metals and toxicity assessment using *Caenorhabditis elegans* in sediments from the Magdalena River, Colombia. *Environ. Pollut.* **2016**, *212*, 238–250. [[CrossRef](#)]
49. Tejeda-Benítez, L.; Noguera-Oviedo, K.; Aga, D.S.; Olivero-Verbel, J. Toxicity profile of organic extracts from Magdalena River sediments. *Environ. Sci. Pollut. Res.* **2018**, *25*, 1519–1532. [[CrossRef](#)] [[PubMed](#)]
50. Molares, B.R. Clasificación e identificación de las componentes de marea del Caribe colombiano. *Boletín Científico CIOH* **2004**, *24*, 105–114. [[CrossRef](#)]
51. Restrepo, J.D.; López, S.A. Morphodynamics of the Pacific and Caribbean deltas of Colombia, South America. *J. S. Am. Earth Sci.* **2008**, *25*, 1–21. [[CrossRef](#)]
52. Pérez, R.A.; Ortiz, R.J.C.; Bejarano, A.L.F.; Otero, D.L.; Restrepo, L.J.C.; Franco, H.A. Sea breeze in the Colombian Caribbean coast. *Atmósfera* **2018**, *31*, 389–406. [[CrossRef](#)]
53. Bedoya-Soto, J.M.; Poveda, G.; Trenberth, K.E.; Vélez-Upegui, J.J. Interannual hydroclimatic variability and the 2009–2011 extreme ENSO phases in Colombia: From Andean glaciers to Caribbean lowlands. *Theor. Appl. Clim.* **2019**, *135*, 1531–1544. [[CrossRef](#)]
54. Cai, W.; McPhaden, M.; Grimm, A.; Rodrigues, R.; Taschetto, A.; Garreaud, R. Climate impacts of the El Niño–Southern Oscillation on South America. *Nat. Rev. Earth Environ.* **2020**, *1*, 215–231. [[CrossRef](#)]
55. Vega, M.J.; Alvarez-Silva, O.; Restrepo, J.C.; Ortíz, J.C.; Otero, L.J. Interannual variability of wave climate in the Caribbean Sea. *Ocean Dyn.* **2020**, *70*, 965–976. [[CrossRef](#)]
56. Higgins, A.; Otero, L.; Restrepo, J.C.; Álvarez, O. Variabilidad estacional de la interacción oleaje-corriente y dinámica de la cuña salina en la desembocadura del Delta del río Magdalena. In *Libro de Resúmenes Extendidos XVI Senalmar*; INVEMAR-ACIMAR, Colombia, Ed.; 2017; pp. 76–80.
57. Higgins, A.; Restrepo, J.C.; Otero, L.; Ortiz, J.C.; Conde, M. Vertical distribution of suspended sediment in the mouth area of the Magdalena River, Colombia. *Lat. Am. J. Aquat. Res.* **2017**, *45*, 724–736. [[CrossRef](#)]

58. Maretec. Mohid Water [Internet]. Mohid Official Webpage. 2020. Available online: http://www.mohid.com/pages/models/mohidwater/mohid_water_home.shtml (accessed on 18 December 2023).
59. Martins, F.; Neves, R.; Leitao, P.; Silva, A. 3D modeling in the Sado estuary using a new generic vertical discretization approach. *Oceanol. Acta* **2001**, *24*, 51–62. [CrossRef]
60. Arakawa, A. Computational design for long-term numerical integration of the equations of fluid motion: Two-dimensional incompressible flow. Part I. *J. Comput. Phys.* **1966**, *1*, 119–143. [CrossRef]
61. Leendertse, J.J. *Aspects of a Computational Model for Long-Period Water-Wave Propagation*; RAND Corporation: Santa Monica, CA, USA, 1967.
62. Abbott, M.B.; Damsgaard, A.; Rodenhuis, G.S. System 21, Jupiter, a design system for two-dimensional nearly horizontal flows. *J. Hydraul. Res.* **1973**, *11*, 1–28. [CrossRef]
63. Canuto, V.M.; Howard, A.; Cheng, Y.; Dubovikov, M.S. Ocean turbulence I: One-point closure model—Momentum and heat vertical diffusivities. *J. Phys. Oceanogr.* **2001**, *31*, 1413–1426. [CrossRef]
64. Willmott, C.J.; Ackleson, S.G.; Davis, R.E.; Feddema, J.J.; Klink, K.M.; Legates, D.R.; O'Donnell, J.; Rowe, C.M. Statistics for the evaluation and comparison of models. *J. Geophys. Res. Oceans* **1985**, *90*, 8995–9005. [CrossRef]
65. Geyer, W.R.; Scully, M.E.; Ralston, D.K. Quantifying vertical mixing in estuaries. *Environ. Fluid Mech.* **2008**, *8*, 495–509. [CrossRef]
66. Simpson, J.; Crisp, D.; Hearn, C. The shelf-sea fronts: Implications of their existence and behaviour and discussion. *Philos. Trans. R. Soc. London. Ser. A Math. Phys. Sci.* **1981**, *302*, 531–546.
67. MacKay, H.; Schumann, E. Mixing and circulation in the Sundays River estuary, South Africa. *Estuar. Coast Shelf Sci.* **1990**, *31*, 203–216. [CrossRef]
68. Ralston, D.K.; Geyer, W.R.; Lerczak, J.A.; Scully, M. Turbulent mixing in a strongly forced salt wedge estuary. *J. Geophys. Res. Oceans* **2010**, *115*, 12024. [CrossRef]
69. IDEAM. Serie de Caudal Medio Diario. Periodo 23/07/1940 y 31/12/2015. Estación Limnimétrica CALAMAR [29037020]. Departamento de Bolívar, Municipio Calamar [Internet]. Available online: <http://dhime.ideam.gov.co/atencionciudadano/> (accessed on 18 December 2023).
70. Pernot, P.; Savin, A. Probabilistic performance estimators for computational chemistry methods: The empirical cumulative distribution function of absolute errors. *J. Chem. Phys.* **2018**, *148*, 241707. [CrossRef]
71. Wischik, D. Foundations of Data Science [Internet]. University of Cambridge. 2020. Available online: <https://www.youtube.com/watch?v=JrS1ajLqMZQ&list=PLknxdt7zG11O5BV8ipHD30dnupEk-tKjn&index=24> (accessed on 18 December 2023).
72. Thorn, M. Coastal and estuarine sediment dynamics by K.R. Dyer. Wiley, Chichester, 1986. No. of pages: 358. *Geol. J.* **1987**, *22*, 169. Available online: <https://onlinelibrary.wiley.com/doi/abs/10.1002/gj.3350220210> (accessed on 18 December 2023). [CrossRef]
73. Pritchard, D.W. Estuarine Classification—A Help or a Hindrance. In *Estuarine Circulation*; Neilson Bruce, J., Kuo, A.B.J., Eds.; Humana Press: Totowa, NJ, USA, 1989; pp. 1–38. [CrossRef]
74. Holford, J.M.; Linden, P.F. Turbulent Mixing in a Stratified Fluid. *Dyn. Atmos. Ocean.* **1999**, *30*, 173–198. Available online: <https://www.sciencedirect.com/science/article/pii/S0377026599000251> (accessed on 18 December 2023). [CrossRef]
75. Read, J.S.; Hamilton, D.P.; Jones, I.D.; Muraoka, K.; Winslow, L.A.; Kroiss, R.; Wu, C.H.; Gaiser, E. Derivation of lake mixing and stratification indices from high-resolution lake buoy data. *Environ. Model. Softw.* **2011**, *26*, 1325–1336. [CrossRef]
76. Burchard, H.; Hofmeister, R. A dynamic equation for the potential energy anomaly for analysing mixing and stratification in estuaries and coastal seas. *Estuar. Coast. Shelf Sci.* **2008**, *77*, 679–687. Available online: <https://www.sciencedirect.com/science/article/pii/S0272771407004945> (accessed on 18 December 2023). [CrossRef]
77. Hamada, T.; Kim, S. Stratification potential-energy anomaly index standardized by external tide level. *Estuar. Coast. Shelf Sci.* **2020**, *250*, 107138. Available online: <https://www.sciencedirect.com/science/article/pii/S0272771420308696> (accessed on 18 December 2023). [CrossRef]
78. Zhang, Z.; Cui, B.; Zhao, H.; Fan, X.; Zhang, H. Discharge–salinity relationships in Modaomen waterway, Pearl River estuary. *Procedia Environ. Sci.* **2010**, *2*, 1235–1245. Available online: <https://www.sciencedirect.com/science/article/pii/S1878029610001672> (accessed on 18 December 2023). [CrossRef]
79. Gisen, J.I.A.; Savenije, H.H.G.; Nijzink, R.C. Revised predictive equations for salt intrusion modelling in estuaries. *Hydrol. Earth Syst. Sci.* **2015**, *19*, 2791–2803. [CrossRef]
80. Gong, W.; Shen, J. The response of salt intrusion to changes in river discharge and tidal mixing during the dry season in the Modaomen Estuary, China. *Cont. Shelf Res.* **2011**, *31*, 769–788. [CrossRef]
81. Liu, W.C.; Chen, W.B.; Cheng, R.T.; Hsu, M.H.; Kuo, A.Y. Modeling the influence of river discharge on salt intrusion and residual circulation in Danshuei River estuary, Taiwan. *Cont. Shelf Res.* **2007**, *27*, 900–921. [CrossRef]
82. Sirviente, S.; Sánchez-Rodríguez, J.; Gomiz-Pascual, J.J.; Bolado-Penagos, M.; Sierra, A.; Ortega, T.; Álvarez, O.; Forja, J.; Bruno, M. A numerical simulation study of the hydrodynamic effects caused by morphological changes in the Guadalquivir River Estuary. *Sci. Total Environ.* **2023**, *902*, 166084. [CrossRef]
83. de Jonge, V.N.; Schuttelaars, H.M.; van Beusekom, J.E.; Talke, S.A.; de Swart, H.E. The influence of channel deepening on estuarine turbidity levels and dynamics, as exemplified by the Ems estuary. *Estuar. Coast. Shelf Sci.* **2014**, *139*, 46–59. Available online: <https://www.sciencedirect.com/science/article/pii/S0272771413005544> (accessed on 18 December 2023). [CrossRef]
84. Li, X.; Cai, Y.; Liu, Z.; Mo, X.; Zhang, L.; Zhang, C.; Cui, B.; Ren, Z. Impacts of river discharge, coastal geomorphology, and regional sea level rise on tidal dynamics in Pearl River Estuary. *Front. Mar. Sci.* **2023**, *10*, 1065100. [CrossRef]

85. Torres, R.R.; Tsimplis, M.N. Sea-level trends and interannual variability in the Caribbean Sea. *J. Geophys. Res. Oceans* **2013**, *118*, 2934–2947. [[CrossRef](#)]
86. Krvavica, N.; Ružić, I. Assessment of Sea-Level Rise Impacts on Salt-Wedge Intrusion in Idealized and Neretva River Estuary. *arXiv* **2020**, arXiv:2001.04765. [[CrossRef](#)]
87. Leung, A.T.Y.; Stronach, J.; Matthieu, J. Modelling behaviour of the saltwedge in the fraser river and its relationship with climate and man-made changes. *J. Mar. Sci. Eng.* **2018**, *6*, 130. [[CrossRef](#)]
88. Burchard, H.; Baumert, H. The Formation of Estuarine Turbidity Maxima Due to Density Effects in the Salt Wedge. A Hydrodynamic Process Study. *J. Phys. Oceanogr.* **1998**, *28*, 309–321. Available online: https://journals.ametsoc.org/view/journals/phoc/28/2/1520-0485_1998_028_0309_tfoetm_2.0.co_2.xml (accessed on 18 December 2023). [[CrossRef](#)]
89. Kappenberg, J.; Grabemann, I. Variability of the Mixing Zones and Estuarine Turbidity Maxima in the Elbe and Weser Estuaries. *Estuaries* **2001**, *24*, 699–706. [[CrossRef](#)]
90. Ralston, D.K.; Geyer, W.R.; Warner, J.C. Bathymetric controls on sediment transport in the Hudson River estuary: Lateral asymmetry and frontal trapping. *J. Geophys. Res. Oceans* **2012**, *117*, 1–21. [[CrossRef](#)]
91. Jay, D.A.; Orton, P.M.; Chisholm, T.; Wilson, D.J.; Fain, A.M.V. Particle trapping in stratified estuaries: Consequences of mass conservation. *Estuaries Coasts* **2007**, *30*, 1095–1105. [[CrossRef](#)]
92. Gregory, J.; O'Melia, C.R. Fundamentals of flocculation. *Crit. Rev. Environ. Control* **1989**, *19*, 185–230. [[CrossRef](#)]
93. Sholkovitz, E. Flocculation of dissolved organic and inorganic matter during the mixing of river water and seawater. *Geochim. Cosmochim. Acta* **1976**, *40*, 831–845. [[CrossRef](#)]
94. Eisma, D. Flocculation and de-flocculation of suspended matter in estuaries. *Neth. J. Sea Res.* **1986**, *20*, 183–199. [[CrossRef](#)]
95. Deng, Z.; He, Q.; Manning, A.J.; Chassagne, C. A laboratory study on the behavior of estuarine sediment flocculation as function of salinity, EPS and living algae. *Mar. Geol.* **2023**, *459*, 107029. [[CrossRef](#)]

Disclaimer/Publisher's Note: The statements, opinions and data contained in all publications are solely those of the individual author(s) and contributor(s) and not of MDPI and/or the editor(s). MDPI and/or the editor(s) disclaim responsibility for any injury to people or property resulting from any ideas, methods, instructions or products referred to in the content.